Cyclostratigraphic age constraining for Quaternary sediments in the Makarov Basin of the western Arctic Ocean using manganese variability

Kwangkyu Park[1,2], Jung-Hyun Kim[1], Hirofumi Asahi[1], Leonid Polyak[3], Boo-Keun Khim[2], Michael Schreck[1,4], Frank Niessen[5], Gee Soo Kong[6], Seung-Il Nam[1,*]

[1]*Division of Polar Paleoenvironment*, *Korea Polar Research Institute*, *26 Songdomirae-ro*, *Yeonsu-gu*, *Incheon 21990*, *Republic of Korea*

[2]*Department of Oceanography*, *Pusan National University*, *2 Busandaehak-ro 63beon-gil*, *Geumjeong-gu*, *Busan*, *46241*, *Republic of Korea*

[3]*Byrd Polar and Climate Research Center*, *Ohio State University*, *Columbus, OH 43210*, *USA*

[4]*The Arctic University of Tromsø, Tromsø*, *Norway*

[5]*Alfred Wegener Institute for Polar and Marine Research*, *Am Handelshafen 12*, *27570 Bremerhaven*, *Germany*

[6]*Korea Institute of Geoscience and Mineral Resources*, *124 Gwahak-ro*, *Yuseon-gu*, *Daejeon 34132*, *Republic of Korea*

Submitted to Quaternary Geochronology

*Corresponding author

E-mail address: sinam@kopri.re.kr

Abstract

The Quaternary paleoenvironmental history of the Arctic Ocean remains uncertain, mainly due to the limited chronological constraints, especially beyond the ^{14}C dating limits of accelerator mass spectrometry (AMS). The difficulty in establishing a reliable chronostratigraphy is mainly attributed to low sedimentation rates and diagenetic sediment changes, resulting in very poor preservation of microfossils and altered paleomagnetic records. In the absence of independent chronostratigraphic data, the age model of the Pleistocene sediments of the Arctic Ocean was mainly based on cyclostratigraphy, which is related to climate changes on orbital time scales. In this study, we used the Mn/Al record measured from the sediment core ARA03B-41GC retrieved from the Makarov Basin in the western Arctic Ocean. In general, the Mn/Al variation was well tuned to the LR04 curve under different assumptions for computational correlation. Regardless of assumptions, our computational approach led to similar ages of about 600–1,000 ka for the bottom part of the core. These age models were up to about 200 ka older than those derived from lithostratigraphic approaches. Interestingly, our new age models show that the Ca/Al peak, a proxy for the detrital inputs from the Laurentide Ice Sheet, first occurred about 150 ka earlier than those previously proposed. Therefore, our results suggest that the glaciers in northern North America developed more extensively at about 810 ka than in earlier glacial periods, and influenced the sedimentary and paleoceanographic environments of the Arctic Ocean much earlier than previously thought. In order to establish a more comprehensive age model, more work is needed to validate our findings with different sediment cores recovered from the western Arctic Ocean.

Keywords: cyclostratigraphy, manganese, western Arctic Ocean, Laurentide Ice Sheet, glacial-interglacial cycles

1. Introduction

Establishing a reliable chronostratigraphy for Arctic Ocean sediments is most important for the reconstruction of high-resolution Quaternary paleoceanographic and cryospheric environments (e.g., Jakobsson et al., 2000; O'Regan et al., 2008; Polyak et al., 2009; Stein et al., 2010a). However, the chronostratigraphic estimates for Arctic sediment records are still highly tentative and present challenges to precise stratigraphic constraints. These difficulties are mainly attributed to very low sedimentation rates in the Arctic Ocean, resulting in various diagenetic imprints on sediments, including a limited presence of microfossils (e.g., Spielhagen et al., 2004; Polyak et al., 2009). For example, the occurrence of calcareous foraminiferal tests in the Arctic sediments is limited to relatively warm periods of the last few interglacials (e.g., Adler et al., 2009; Polyak et al., 2013). The use of paleomagnetic chronology is also questionable, as the nature of variations in magnetic polarity in Arctic sediment records is still not fully understood (Jakobsson et al., 2001; Spielhagen et al., 2004; Channell and Xuan, 2009; Xuan et al., 2012).

The current age models for western Arctic sediments have generally been compiled on the basis of accelerator mass spectrometry (AMS) ^{14}C dating in the uppermost strata, cyclic stratigraphic features associated with glacial-interglacial variations, and bio- and lithostratigraphic markers (e.g., Polyak et al., 2004, 2009; Adler et al., 2009; Stein et al., 2010a; Schreck et al., 2018; Wang et al., 2018). The cyclicity is accentuated by manganese (Mn) enrichment, which caused a distinct brown color in interglacial and major interstadial sediment layers. This is evidently seen at the stratigraphic interval corresponding to the period of "glacial Pleistocene," when large continental glaciers developed around the Arctic Ocean in the middle to late Quaternary (Polyak et al., 2013; Dipre et al., 2018). However, the identification of climatic cycles beyond the middle Pleistocene (>780 ka) is even weaker, leading to ambiguities in the reconstruction of long-term paleoclimatic environments. Accordingly, age models beyond the middle Pleistocene are still being revised. For example, the age model constrained for Northwind Ridge sediments according to Mn-based cyclostratigraphy (Polyak et al., 2013) has recently been modified by the Sr isotope approach (Dipre et al., 2018).

In this study, we investigate a sediment core with distinct lithostratigraphic cyclicity to establish Quaternary cyclostratigraphy in the Makarov Basin off the East Siberian margin in the western Arctic Ocean. We apply both visual and computational correlations of the Mn/Al record to the global benthic oxygen isotope stack (LR04; Lisiecki and Raymo, 2005). By comparing different age models, we show that a computational approach can be used to provide a consistent age model under different assumptions over the last ~1,000 ka in the western Arctic Ocean.

2. Background

2.1. Study area

The Arctic Ocean is a semi-enclosed ocean surrounded by continents including North America, Eurasia, Greenland, and the Canadian Arctic Archipelago (Fig. 1). Beyond the broad and shallow shelf areas of the Eurasian Arctic coasts, the deep basins are divided by several ridges, including Lomonosov Ridge in the central Arctic Ocean, the Alpha–Mendeleev Ridge Complex in the western Arctic Ocean, and the Gakkel Ridge in the Eastern Arctic Ocean (Fig. 1). In the Amerasian Basin, the Makarov Basin is bounded by the Alpha–Mendeleev and Lomonosov ridges, as well as the Siberian and Canadian shelves, with a maximum depth of ~3,950 m (Nowaczyk et al., 2001). This wedge-shaped basin is 500 km wide along the East Siberian Shelf, which narrows to the north, and consists of the Wrangel and Siberia Abyssal plains. The broad and relatively shallow southern plain with a maximum depth of ~2,800 m is known as Podvodnikov in Russian (Sorokin et al., 1999).

The wind-driven modern surface current systems in the Arctic Ocean are dominated by the anti-cyclonic Beaufort Gyre and the Transpolar Drift, which transport surface water masses, including sea ice, from the Eurasian shelves toward the Fram Strait (Fig. 1). Both the main currents mainly occupy the Amerasian and Eurasian basins, respectively. The study area in the Makarov Basin is mainly under the influence of the Beaufort Gyre.

2.2. Sediment stratigraphy in the Arctic Ocean

Previous studies on sediment cores and submarine topography in the Arctic Ocean, which focused mainly on margins and geographic features such as ridges and plateaus, showed paleoceanographic changes and glacial history during the late Quaternary (e.g., Polyak et al., 2004, 2007; Jakobsson et al., 2008, 2010, 2014; Adler et al., 2009; Stein et al., 2010a; Niessen et al., 2013; Schreck et al., 2018). However, continuous sediment records for paleoenvironmental reconstructions in the surrounding marginal areas and topographic highs are still rare due to sediment perturbations, including glacial activities (diamicton deposit and erosion), mass waste (e.g., landslides), and hiatus. This leads to technical limitations of stratigraphic inter-core correlations in the heavily ice-covered Arctic Ocean. In contrast, sediment records in Arctic deep basins are more appropriate for studying the long-term history of the Quaternary Arctic Ocean due to relatively low sedimentation rates (Darby et al., 2006). In the Amerasian Basin, standard lithostratigraphic (SL) units were first established using sediment cores collected from Ice Island (T3; Clark et al., 1980), which were commonly used for sediment core correlations in the western Arctic Ocean (Stein et al., 2010b). Because of the unavailability of the archived sediments and the state-of-the-art analytical results of T3 cores, a new sediment core (PS72/392-5) near the T3 core site (FL-224) was re-cored to develop applicable multi-proxies for paleoceanographic reconstruction in the western Arctic (Stein et al., 2010b). This has provided opportunities to establish correlations between inter-cores based on nondestructive measurements, experimental analyses, and lithologic features obtained from various sediment records (e.g., Matthiessen et al., 2010; Meinhardt et al., 2014; Dong et al., 2017; Schreck et al., 2018; Wang et al., 2018). It is also worthwhile to note that while sediment cores in the Arctic Ocean are mostly relatively short, the Arctic Coring Expedition (ACEX) conducted by the Integrated Ocean Drilling Program (IODP) on the Lomonosov Ridge was the first to provide a long sediment core covering most of the Cenozoic (Backman et al., 2008). Based on a multidisciplinary approach involving biostratigraphy, magnetostratigraphy, and lithostratigraphy, a stratigraphy for the last ~1,200 ka was established in the central Arctic Ocean (O'Regan et al., 2008). However, it is unknown whether this stratigraphy can be applied to the stratigraphic correlation in the western Arctic Ocean.

The stratigraphy for the Termination II (marine isotope stages (MIS) 5/6) to the Holocene, during the last 130 ka, is relatively well constrained in the western Arctic Ocean based on AMS ^{14}C dating and lithological characteristics (e.g., O'Regan et al., 2008; Adler et al., 2009; Stein et al., 2010a; Wang et al., 2018). The MIS stages are subdivided mainly based on the occurrence of (dark) brown layers, generally referred to as B# in ascending order from top to bottom, and beige to olive-gray layers (Fig. S1). In addition, pink–white (PW) intercalated layers of prominently increased ice-rafted debris (IRD) are commonly used as markers for stratigraphic correlation. For example, it is assumed that PW2, which generally occurs between B6 (6th brown layer) and B7 (7th brown layer), corresponds to MIS 5.4 (Stein et al., 2010a; Schreck et al., 2018). Due to a large amount of IRD, which consists of detrital carbonate transported from the northern Canadian Arctic Archipelago (Bischof et al., 1996; Vogt 1997; Phillips and Grantz, 2001), the PW layers were used as an indicator of the advance and retreat of the Laurentide Ice Sheet (LIS) in North America. Beyond Termination II, i.e., before the late Pleistocene, the age model is hampered by the lack of reliable age constraints (e.g., Dong et al., 2017; Schreck et al., 2018). Existing chronological information for the middle Pleistocene (130–780 ka) is based mainly on lithologic features including alternations of brown and gray layers and stratigraphic markers such as the PW1 layer. For example, Dong et al. (2017) proposed an age model established by the stratigraphic correlation of core ARC4–BN05 with core PS72/392-5 (Stein et al., 2010a). However, their models only covered ages up to MIS 16, which is discussed in section 5.2.

2.3. Sedimentary Mn fluctuations

Modern Mn sources in the Arctic Ocean are mainly coastal erosion and river discharge, whereas inputs from hydrothermal vents, the atmosphere, groundwater, and oceans are insignificant (Macdonald and Gobeil, 2012). Although much of Mn is primarily trapped in shelf areas near its main sources, its terminal sink is the basin, which accounts for more than three-fourths of the total Mn sink (Löwemark et al., 2014). The Mn delivered to shelves and its subsequent transport to basins was highly regulated by the environmental changes of the glacial-interglacial, i.e., sea level, sea ice, current, and river discharge. Mn supplies were likely weaker during cold glacial/stadial periods than during warm interglacial/interstadial periods, as low sea-levels, larger continental ice sheets, inactive surface currents, and thick/perennial sea-ice covers obstructed coastal erosion and riverine input to shelves and subsequent transports to basins. Accordingly, the alternations of Mn-poor and -rich layers are considered as glacial-interglacial and possibly stadial–interstadial cycles. Post-depositional processes can cause Mn remobilization, particularly in organic-rich layers; however, this diagenetic process is likely to be reduced in deep sediments with very low organic matter (März et al., 2011; Löwemark et al., 2014).

In order to use cyclic Mn layers as a stratigraphic tool, it is important to distinguish them from brown and beige layers. At the continental margins of the Arctic Ocean, the Mn signals of sediment could be attenuated due to high sedimentation rates via glacier sediment supplies, or they could be perturbed by glacial erosion and gravitational deposition (e.g., Polyak et al., 2004; Adler et al., 2009; Park et al., 2017; Schreck et al., 2018). In contrast, deep-sea deposits have lower sedimentation rates due to their long distance from sediment sources (e.g., Polyak et al., 2009; Stein et al., 2010a; Schreck et al., 2018), resulting in condensed Mn-rich layers under thick perennial sea-ice covers (e.g., Wang et al., 2018). At topographic highs such as shallow margins, ridges, and plateaus, erosional events have often disturbed sediment records, hampering the identification of Mn-enriched layers (e.g., Polyak et al., 2004; O'Regan et al., 2008; Jakobsson et al., 2008, 2010).

Based on the presence of the sedimentary Mn layer, a stratigraphic tool was established from a sediment core retrieved from the central Lomonosov Ridge (Jakobsson et al., 2000). The cyclic sediment sequence was correlated with a low-latitude $\delta^{18}O$ stack (Bassinot et al., 1994) based on the assumption that Mn-enriched layers correspond to warm interglacial/interstadial periods. Additional stratigraphic approaches using paleomagnetism, cyclostratigraphy, and biostratigraphy have supported the potential of Mn-based stratigraphy to solve difficulties in establishing the age model (Jakobsson et al., 2000, 2001; Backman 2004). In the western Arctic Ocean, sedimentary Mn fluctuations are highly distinguishable, as the contrast of lithological features varies distinctly between the glacial and interglacial periods (Polyak and Jakobsson, 2011; Schreck et al., 2018). However, Mn-based stratigraphic studies have so far mainly been confined to the Lomonosov Ridge (e.g., Löwemark et al., 2012, 2014).

3. Materials and methods

3.1. Core sampling and measurements

A 4.65 m long sediment core (ARA03B-41GC02; hereafter 41GC) was taken using a gravity corer from the Makarov Basin near the bottom of the Mendeleev Ridge slope (82°19'22" N, 171°34'17" E, 2,710 m water depth) during the 2012 Arctic expedition with the research vessel (RV) Araon (Fig. 1). Multiple cores (ARA03B-41MUC) were also collected at the same site for better recovery of surficial sediments. Wet bulk density (WBD) and magnetic susceptibility (MS) were measured on board the RV Araon at 10 mm intervals on whole core sections using a standard multi-sensor core logger (MSCL; GEOTEK, UK; Schreck et al., 2018).

Split cores were macroscopically described and scanned for X-ray fluorescence (XRF) and color reflectance (L*, a*, and b*). XRF measurements were conducted for semi-quantitative elemental composition analysis focusing on Al, Ca, and Mn using an Avaatech core scanner at the Korea Institute for Geoscience and Mineral Resources (KIGAM, South Korea). Measurements were performed at 5 mm steps, and elemental concentrations were specified as counts (e.g., Schreck et al., 2018). The elemental contents were normalized by Al (e.g., Calvert and Pedersen, 2007; Schreck et al., 2018). Color reflectance including lightness, redness, and yellowness was measured at 0.5 cm intervals using a Konica Minolta color spectrophotometer CM-2600d with a 0.5 cm aperture.

For further analysis, subsamples were taken at 1 cm intervals, freeze-dried, and analyzed for sand fraction contents (> 63 μm) for every 2 cm. At the same intervals, the grain size was analyzed for the mud fraction (< 63 μm) using Malvern Mastersize 3000. After removal of organic matters which had been treated with hydrogen peroxide (10 %, 50 ℃, 24 h), the wet-sieved samples were disaggregated and dispersed using an ultrasonicator and then analyzed with a measurement time of 15 seconds at 10-20 % obscuration level. In addition, AMS ^{14}C measurements (Table 1) on planktic foraminifera *Neogloboquadrina pachyderma* sinistral (150–250 μm) were conducted at five core depth intervals of 0–1 cm, 6–7 cm, 10–11 cm, and 19–20 cm for 41GC and 0–1 cm for 41MUC at Beta Analytic (Miami, USA). The radiocarbon age was calibrated to calendar ages using CALIB 7.10 (Marine13, Reimer et al., 2013); the local reservoir correction (ΔR) has been set as 0 due to uncertainties in reservoir ages in the

Arctic Ocean water (e.g., Hanslik et al., 2010; Park et al., 2017).

3.2. Visual and computational correlations

Lithological features, including sediment color, MS, WBD, and sand fraction content, were used for visual (non-computational) correlations with previously published stratigraphic records for the western Arctic Ocean (e.g., Adler et al., 2009; Polyak et al., 2009; Stein et al., 2010a, b; Dong et al., 2017; Schreck et al., 2018) and the Lomonosov Ridge (Jakobsson et al., 2000; O'Regan et al., 2008). From these records, the core ARC4-BN05 (Dong et al., 2017), retrieved from the Canadian Basin rather than from a ridge, can be considered to be the most compatible with core 41GC in terms of stratigraphic coverage and the sedimentary environment in the western Arctic Ocean (Fig. 1). Thus, a visual correlation was performed by comparing the brown layers of core 41GC with those of core ARC4-BN05 (Table 2; VC01). Another visual correlation was conducted based on the brown layers of core 41GC and LR04 (Table 2; VC02).

To establish a more objective cyclostratigraphic-based chronology beyond the late Pleistocene, the computational correlations of the Mn/Al record of core 41GC with LR04 were performed using a dynamic matching program (Match 2.3.1; Lisiecki and Lisiecki, 2002). The software uses dynamic programming to implement an automated correlation algorithm that finds the best optimal fit between two climatic records (e.g., Lisiecki and Raymo, 2005). For example, in the Arctic Ocean, Marzen et al. (2016) have shown that stacked records can be successfully aligned against LR04 using the Match software. In this study, various stratigraphic horizons, including AMS ^{14}C dates, the PW2 layer between B6 and B7 corresponding to MIS 5.4, and MIS 5/6 and 6/7 boundaries, were used as alternative initial age constraints (Adler et al., 2009; Stein et al., 2010a; Dong et al., 2017). The computational matching of the Mn/Al record to LR04 was performed under different initial age constraints (Table 2; MA01 to MA05).

Here, Match parameters were unified to achieve tunings under the same conditions. Initial and final values were given by corresponding core depths of start and end data, respectively (Table 2). Number of intervals has been set to the default value. In order to obtain relatively free correlations, the penalties for speed and speed change were set to very low values of 0.001 and 0.01 for all models, respectively. In contrast, the tie point penalty was set for all models with a relatively high value (4) for a strict constraint of the tie points, including the ^{14}C ages and MIS boundaries. As with speed-related penalties, the gap penalty has been set to a relatively low value (1).

4. Results

Figure 2 shows the data generated for core 41GC, including the core surface image, the color reflectance (L* and a*), the ratios of Mn/Al and Ca/Al, the logged physical properties (MS and WBD), and the sand content. Based on the visible description, the (dark) brown layers generally consist of soft, muddy sediments with a sharp upper contact and a mottled lower transitional contact. In contrast, interlaminated gray/beige layers are generally denser and relatively sandy, with intermittently visible intercalations of coarse-grained IRD in the millimeter to centimeter scale. Color indices and Mn/Al ratio varied closely, showing 31 cycles in which dark and reddish-brown layers associated with B1–B31 were intercalated with light, yellowish-gray layers (Fig. 2). The MS and WBD values associated with the sand content are higher at the gray layers and the boundary between the brown and gray layers (Fig. 2). Similarly, the Ca/Al ratios shows high values at the brown/gray boundaries, with the first (oldest) peak appearing at the top of the layer B20 (Fig. 2). The PW2 layer represents the highest Ca/Al ratio and the WBD value with increased MS value and sand content (Fig. 2).

Based on the visual correlation of the brown layers of core 41GC with those of the core ARC4-BN05, the first age model VC01 yielded an age of MIS assignment from the MIS 1 to

14/15 boundary (Table 2, Fig. 3). Based on the correlation between the brown layers of core 41GC and LR04, the second visual correlation model VC02 could assign the MIS stages from MIS 5/6 boundary to MIS 28 with a bottom age of 1,014 ka (Table 2, Fig. 4). Since these two age models coincide over the period from MIS 5 to 15, different age models can be generated. Interestingly, regardless of the age constraints used (Table 2), age-depth relationships of the computational correlations between the Mn/Al record of core 41GC and LR04 differed from those of visual correlations (Figs. 5, 6). Similar matching patterns with a core depth below 330 cm were observed in the three computational age models (MA01–MA03), which assumed the lower core bottom age of 1,014 ka (bottom of MIS 28) obtained from VC02. However, there were obvious differences between core depths of 160 and 330 cm depending on the age constraints applied. The age model MA04, which did not have a fixation of the bottom age but applied AMS ^{14}C age constraints, showed a different age-depth trend with the oldest bottom core age of 1,384 ka compared to those of other visual and computational models. In contrast, the age model MA05, which also had no bottom age limit but was set with the constraints of MIS 5/6 and 6/7 boundaries for core depths below 160 cm, showed a similar age-depth pattern to those of age models MA01–MA03 which were constrained with the fixed bottom age.

5. Discussion

Cyclic Quaternary climate changes, accompanied by the growth/retreat of ice sheets in the higher Northern Hemisphere, strongly affected the sedimentary and paleoceanographic environments of the Arctic Ocean through changes in sediment supply, sea-ice and surface productivity, hydrography, and circulation patterns (e.g., Stein, 2008). These changes are well recorded in glaciomarine sediments of core 41GC. The sediment records show approximately 30 pairs of interlaminating gray and brown layers (Fig. 2), which are closely related to glacial-interglacial or major stadial–interstadial cycles. The overall lithostratigraphy is characterized by increased proxy amplitudes and layer thicknesses toward the top of the core (Fig. 2). This pattern may reflect changes in sediment supply as the glaciers of the Northern Hemisphere were intensified during the Pleistocene (e.g., Balco and Rovey, 2010). In particular, proxies such as bulk Ca, WBD, and sand content have been used as indicators of glacial deposits transported to the Arctic Ocean (e.g., O'Regan et al., 2008; Polyak et al., 2009, 2013; Dong et al., 2017; Wang et al., 2018). Based on these proxies, a reasonable chronology of core 41GC is needed for the age-constrained reconstruction of the Arctic glacial history in relation to global climate change.

5.1. Visual approach

Based on the correlations using various parameters including sediment color, texture, physical properties, and Mn and Ca contents, the lithology of core 41GC was well matched with the sediment cores previously studied in the western Arctic Ocean (Adler et al., 2009; Stein et al., 2010b; Dong et al., 2017; Figs. 1, 3, and S1). Using multiple proxies, the upper part of core 41GC can be correlated with core HLY0503-8JPC recovered from the southern foot of the Mendeleev Ridge (Adler et al., 2009; Fig. S1). The advantage of this comparison is that core HLY0503-8JPC has an extended age of the upper Quaternary record through its correlation with the age framework developed by several approaches, including AMS ^{14}C and amino-acid dating, and correlates with the nannofossil and optical-stimulating luminescence age constrained from the Lomonosov Ridge (Adler et al., 2009). However, a chronologic framework is only possible up to MIS 7.

The visual correlation, which is mainly based on the cyclic interlamination of brown and gray layers recorded in core ARC4-BN05 (Dong et al., 2017) taken from the Canada Basin near the Makarov Basin, can extend the age constraints to the middle Pleistocene (VC01; Table 2, Fig. 3). According to this correlation, layers B1-B18 of core 41GC were assigned to MIS 1-

15, assuming that gray layers with high sand content and Ca levels represent glacial intervals, while brown, Mn-enriched layers indicate interglacial periods (Stein et al., 2010a, b; Dong et al., 2017). However, this assumption has not been proven as an independent stratigraphic marker. Some previous studies for the late Pleistocene showed that brown layers are associated with conditions of maximum interglacials and major interstadials such as MIS 3, 5.1, and 5.3 (Adler et al., 2009; Stein et al., 2010a; Schreck et al., 2018). Similarly, beige/gray layers represent individual stadials or prominent pulses of meltwater and iceberg discharge events rather than glacial periods. This pattern is also found in the middle Pleistocene record, which complicates the relationship between the lithostratigraphic records and paleoclimatic cyclicities on global scales.

Our visual correlation of core 41GC Mn/Al records was established with LR04 (VC02) at the top of the middle Pleistocene (130 ka) to cover a period longer than the age model VC01 (Fig. 4; Table 2). In the absence of independent age constraints, this correlation was based on the assumption that the Mn/Al peaks coincided with climatically warm periods (e.g., Jakobsson et al., 2000; Wang et al., 2018). Based on this approach, the bottom of core 41GC has been extended to MIS 28, 982–1014 ka (Fig. 4). When the combined age model VC01-02 was applied to compare the Mn/Al record of core 41GC with LR04, the Mn/Al ratios were generally high during interglacials, but low during glacials (Fig. S2). The Mn/Al variation, however, did not correspond well in detail to LR04, with difficulties in assigning each Mn/Al peak to MIS substages. This is likely due to uncertainties in the age constraints that applied to the age model VC02 (Table 2). Similar difficulties in the direct correlation between Mn/Al ratios and LR04 have been reported for the Northwind and Alpha ridges (Polyak et al., 2013; Wang et al., 2018).

5.2. Computational approach

Previous stratigraphic studies in the Canada Basin and Northwind Ridge (Stein et al., 2010a, b; Dipre et al., 2018) showed that the distinct interlaminations of the brown–beige layers blurred and homogenized in older strata, making it difficult to identify. According to the Sr isotopic dating in the Northwind Ridge (Dipre et al., 2018), the boundary between cyclic interlamination unit and homogenous dark brown unit placed at the end of the Early Pleistocene (Brunhes-Matuyama boundary; ~780 ka). However, this boundary may be older (i.e. before ~780 ka) in the Amerasian Basin (Stein et al., 2010a). In an attempt to solve this problem, we performed an additional computational correlation of the WBD data between core 41GC and ACEX (O'Regan et al., 2008). It appears that both WBD records vary at the same time to determine the bottom age of 1,168 ka (Fig. S2). When using this WBD-based age model to compare the Mn/Al record of core 41GC with LR04, the occurrence of the Mn-enriched layers, however, did not match the anticipated interglacials (Fig. S3). This suggests that the WBD correlation between the western Arctic Ocean and the central or eastern Arctic Ocean may not be adequate due to differences in the sources and depositional process of the sediment (e.g. Sellen et al., 2010). The clockwise Beaufort Gyre in the Amerasian Basin transports sediments mainly from the margin of the western Arctic, whereas the central and eastern Arctic Ocean receives sediments mainly from the Eurasian marginal seas, such as the Barents and Kara seas, mainly through the Transpolar Drift. On the Lomonosov Ridge, for example, there is a close correlation between WBD and sand with coarse silt fraction (20-125 μm), which has a strong positive coefficient than that of sand fraction only (O'Regan et al., 2019). This correspondence with previous studies showed that grain size is the major cause of bulk density variation in downcore (O'Regan et al., 2008, 2014). However, in this study, the sand and coarse silt fraction do not fully explain the overall variability of WBD (Fig. S4 and Table S5), indicating a different depositional environment between the central and western Arctic Ocean. This highlights a strong need for an independent age model of the western Arctic Ocean in accordance with previous studies that defined it as a unique environment (e.g., Polyak and Jakobsson, 2011).

For the development of a cyclostratigraphic correlation between the Mn/Al record and LR04, which is more objective than the visual correlation, we used a computational dynamic matching method (Lisiecki and Lisiecki, 2002). Interestingly, despite the different correlation assumptions, the bottom age-fixed models, MA01-MA03, showed a consistent age-depth relationship between 1,014 (MIS 28) and ~600 ka (MIS 15) (Fig. 6). A similar relationship was derived from MA05, which applied no bottom age fixation. Thus, our computational age models were consistent, at least for the lower part of core 41GC, giving ~1,000 ka for the bottom core age except for MA04 (Fig. 6 and Table 2). However, there were apparent differences between ~600 (MIS 15) and 130 ka (MIS 5/6) depending on the age constraints applied (Table 2). Hence, we examined the factors that caused the differences among the computational correlations to the middle Pleistocene.

Previous studies based on visual correlation have presented different age models for sediment records in the western Arctic Ocean during the Pleistocene. These age models tentatively assign massive sandy and lighter layers to peak glacial periods, e.g., MIS 10, 12, and 16 (Stein et al., 2010a, b). In addition, the boundary between the interlaminated and underlying non-stratified thick dark brown units in the western Arctic Ocean was considered to be older than ~500 ka (Polyak et al., 2009) or ~750 ka (Stein et al., 2010a). More recently, however, the age of this boundary was changed to the upper early Pleistocene (~800 ka) in the Northwind Ridge (Dipre et al., 2018). Accordingly, the chronologic constraints likely have to be further refined, especially for periods older than the late Pleistocene. In this context, our computational approach shows the possibility of establishing an alternative age model, especially for the middle to early Pleistocene, and the strong relationships between the Mn/Al record of core 41GC and LR04. Therefore, we propose a combined age model derived from the visual age model VC01 for the late Pleistocene and from the computational Mn/Al-LR04, MA05 for the middle to early Pleistocene.

5.3. Implications of newly developed age models for the Arctic glacial history

The most prominent climate changes in the Northern Hemisphere during the Pleistocene are characterized by the growth and retreat of the continental ice sheets. During the early Pleistocene glacial periods, relatively small ice sheets existed sporadically in Western and Eastern North America (Barendregt and Duk-Rodkin, 2011). The early Pleistocene glaciers gradually extended and eventually merged during the Brunhes Chron (Barendregt and Duk-Rodkin, 2004, 2011; Ehlers and Gibbard, 2007). In addition, the Keewatin Ice Center has expanded broadly and begun to extend the glaciers further north to the Banks Island and the Mackenzie Valley of the North–West Territories, adjacent to the Arctic Ocean, probably since the upper Matuyama (Barendregt and Duk-Rodkin, 2011). These regions are considered to be the source of terrigenous inorganic carbonates in western Arctic Ocean sediments, including IRDs, while the sediments of the eastern Arctic Ocean, far from northern North America and the Canadian Arctic Archipelago, consist mainly of coal, sedimentary rocks, and quartz, but lack of carbonates (Bischof et al., 1996). Therefore, the carbonate sediments in the western Arctic Ocean appear to be related to glacial activities, indicating iceberg calving and meltwater discharge from the LIS that has been extended to the carbonate platform (e.g., Stein et al., 2010a; Dong et al., 2017; Park et al., 2017).

Since the biogenic constituents of total inorganic carbon in the western Arctic sediments are lower, Ca estimated using XRF-core scanning is generally considered to be detrital carbonate in the western Arctic Ocean (Stein et al., 2010a; Dong et al., 2017; Park et al., 2017; Wang et al., 2018). According to conventional lithostratigraphy in the western Arctic Ocean, a prominent Ca peak at ~150 cm of core depth, referred to as PW2 (Figs. 2 and 3), corresponds to MIS 5.4 (Stein et al., 2008, 2010a). However, the transport and deposition mechanism and the exact timing of the PW2 layer are still uncertain (e.g., Schreck et al., 2018). In addition, the first occurrence of a Ca peak in the western Arctic Ocean was considered as MIS 16, i.e. the first "super" glaciation of the Pleistocene (Stein et al., 2010a), but this age constraint was visually estimated as discussed in sections 5.1 and 5.2. As in MA05 and MA01–MA03 (Fig. 7), the first occurrence of Ca peak corresponds to the boundary of MIS 20/21, which is older than the previously reported MIS 16 (Stein et al., 2010a, b; Polyak et al., 2013). Based on the newly proposed age model, the timing of the first Ca peaks at 814 ka seems plausible given the glacial impact of the North American Arctic and the Canadian Arctic Archipelago with a wide carbonate bed during the Matuyama Chron (774-2,595 ka; Cohen and Gibbard, 2019) (Barendregt and Duk-Rodkin, 2004, 2011). Thus, this finding suggests that the first advance of the LIS into the Arctic Ocean occurred at about 814 ka. The first Ca peak corresponds to the mid-Pleistocene transition (MPT) from ~800 to ~1,200 ka when the orbitally paced glacial-interglacial cycles gradually intensified with the amplitude modulation of precession forcing (Imbrie et al., 2011; Hinnov et al., 2013). Based on boron isotope CO_2 data, Chalk et al. (2017) have recently argued that the MPT may be triggered by a change in ice sheet dynamics. In this context, the LIS would also be more extensive and would contribute to an increase in global ice volume since the MPT (Bintanja and van de Wal, 2008; Balco and Rovey, 2010). During this interval, glaciers advanced to the coast adjacent to the Arctic Ocean would be collapsed and the terrestrial carbonate would be carried away in icebergs and eventually transported further westwards via the Beaufort Gyre (e.g. Phillips and Grantz, 2001). As a result, our newly constructed age models can provide alternative evidence for a better understanding of the glacial history in North America and the Canadian Arctic Archipelago during the MPT.

6. Conclusions

In this study, we investigated a sediment core ARA03B-41GC retrieved from the Makarov Basin in the western Arctic Ocean by analyzing MSCL (WBD and MS), color reflectance (L* and a*), XRF-core scanning (Al, Ca, and Mn counts), and contents of sand and mud fractions. The new age model was constrained by applying a computational approach in addition to a more traditional visual approach using the Mn/Al ratios and the brown layers. The computational matching with the LR04 curve represents a consistent relationship between age and depth under various assumptions, indicating ~1,000 ka for the bottom age of the core. However, the visual correlation with the LR04 curve showed that the age of the bottom part of the core was up to ~200 ka younger. Our newly established age models, which were based on computational matching, therefore provided a new age constraint for the first occurrence of a Ca/Al peak at ~810 ka. This indicates that the initial advance of the LIS occurred at the boundary between MIS 20 and 21, which corresponds to the upper Matuyama Chron. Our results are more consistent with terrestrial records than previous studies that suggested the occurrence of the first Ca peak in MIS 16. Nonetheless, our results should be further confirmed on the basis of a similar approach using various sediment cores collected from the western Arctic Ocean.

Acknowledgments

We would like to thank the captain and crew of RV Araon for their excellent support and colleagues (Y.J. Son and Y.J. Joe) of the KOPRI’s Arctic paleoceanography group and Dr. D. Han (Jeju National University) for taking sediment cores during the expedition ARA03B in 2012. This research is funded by the Seed-type Research Program of the Korea Polar Research Institute (No. PE19350 to SIN).

References

Adler, R. E., Polyak, L., Ortiz, J. D., Kaufman, D. S., Channell, J. E., Xuan, C., Grottoli, A. G., Sellén, E., & Crawford, K. A., 2009. Sediment record from the western Arctic Ocean with an improved Late Quaternary age resolution: HOTRAX core HLY0503-8JPC, Mendeleev Ridge. Global and Planetary Change, 68, 18−29.

Backman, J., Jakobsson, M., Løvlie, R., Polyak, L., & Febo, L. A., 2004. Is the central Arctic Ocean a sediment starved basin? Quaternary Science Reviews, 23, 1435−1454.

Backman, J., Jakobsson, M., Frank, M., Sangiorgi, F., Brinkhuis, H., Stickley, C., O'Regan, M., Løvlie, R., Pälike, H., Spofforth, D., Gattacecca, J., Moran, K., King, J., Heil, C., 2008. Age model and core-seismic integration for the Cenozoic Arctic Coring Expedition sediments from the Lomonosov Ridge. Paleoceanography 23, PA1S03, doi:10.1029/2007PA001476.

Balco, G., & Rovey, C. W., 2010. Absolute chronology for major Pleistocene advances of the Laurentide Ice Sheet. Geology, 38, 795−798.

Barendregt, R. W., & Duk-Rodkin, A., 2004. Chronology and extent of Late Cenozoic ice sheets in North America: a magnetostratigraphic assessment. In Developments in Quaternary Sciences (Vol. 2, pp. 1−7). Elsevier.

Barendregt, R. W., & Duk-Rodkin, A., 2011. Chronology and extent of Late Cenozoic ice sheets in North America: a magnetostratigraphical assessment. In Developments in Quaternary Sciences (Vol. 15, pp. 419−426). Elsevier.

Bassinot, F. C., Labeyrie, L. D., Vincent, E., Quidelleur, X., Shackleton, N. J., and Lancelot, Y., 1994. The astronomical theory of climate and the age of the Brunhes-Matuyama magnetic reversal: Earth and Planetary Science Letters, v. 126, p. 91–108.

Bintanja, R., & Van de Wal, R. S. W., 2008. North American ice-sheet dynamics and the onset of 100,000-year glacial cycles. Nature, 454, 869.

Bischof, J., Clark, D. L., & Vincent, J. S., 1996. Origin of ice-rafted debris: Pleistocene paleoceanography in the western Arctic Ocean. Paleoceanography, 11, 743−756.

Calvert, S. E., & Pedersen, T. F., 2007. Chapter fourteen elemental proxies for palaeoclimatic and palaeoceanographic variability in marine sediments: interpretation and application. Developments in Marine Geology, 1, 567−644.

Chalk, T. B., Hain, M. P., Foster, G. L., Rohling, E. J., Sexton, P. F., Badger, M. P., Cherry, S. G., Hasenfratz, A. P., Haug, G. H., Jaccard, S. L., Martínez-García, A., Palike, H., Pancost, R. D., & Wilson, P. A., 2017. Causes of ice age intensification across the Mid-Pleistocene Transition. Proceedings of the National Academy of Sciences, 114, 13114-13119.

Channell, J. E. T., & Xuan, C., 2009. Self-reversal and apparent magnetic excursions in Arctic sediments. Earth and Planetary Science Letters, 284, 124-131.

Clark, D. L., Whitman, R. R., Morgan, K. A., & Mackey, S. D., 1980. Stratigraphy and glacial-marine sediments of the Amerasian Basin, central Arctic Ocean (Vol. 181). Geological Society of America.

Cohen, K. M., & Gibbard, P. L., 2019. Global chronostratigraphical correlation table for the last 2.7 million years, version 2019 QI-500. Quaternary International. Doi: 10.1016/j.quaint.2019.03.009.

Darby, D. A., Polyak, L., & Bauch, H. A., 2006. Past glacial and interglacial conditions in the Arctic Ocean and marginal seas–a review. Progress in Oceanography, 71, 129−144.

Dipre, G. R., Polyak, L., Kuznetsov, A. B., Oti, E. A., Ortiz, J. D., Brachfeld, S. A., Xuan, C., Lazar, K. B., & Cook, A. E., 2018. Plio-Pleistocene sedimentary record from the Northwind Ridge: new insights into paleoclimatic evolution of the western Arctic Ocean for the last 5 Ma. Arktos, 4, 24.

Dong, L., Liu, Y., Shi, X., Polyak, L., Huang, Y., Fang, X., Liu, J., Zou, J., Wang, K., Sun, F., & Wang, X., 2017. Sedimentary record from the Canada Basin, Arctic Ocean:

implications for late to middle Pleistocene glacial history. Climate of the Past, 13, 511.

Ehlers, J., & Gibbard, P. L., 2007. The extent and chronology of Cenozoic global glaciation. Quaternary International, 164, 6−20.

Hanslik, D., Jakobsson, M., Backman, J., Björck, S., Sell_en, E., O'Regan, M., Fornaciari, E., Skog, G., 2010. Quaternary Arctic Ocean sea ice variations and radiocarbon reservoir age corrections. Quaternary Science Reviews, 29, 3430−3441.

Hinnov, L. A., 2013. Cyclostratigraphy and its revolutionizing applications in the earth and planetary sciences. Geological Society of America Bulletin, 125, 1703−1734.

Jakobsson, M., Løvlie, R., Al-Hanbali, H., Arnold, E., Backman, J., & Mörth, M., 2000. Manganese and color cycles in Arctic Ocean sediments constrain Pleistocene chronology. Geology, 28, 23−26.

Jakobsson, M., Løvlie, R., Arnold, E. M., Backman, J., Polyak, L., Knutsen, J. O., & Musatov, E., 2001. Pleistocene stratigraphy and paleoenvironmental variation from Lomonosov Ridge sediments, central Arctic Ocean. Global and Planetary Change, 31, 1−22.

Jakobsson, M., Polyak, L., Edwards, M., Kleman, J., & Coakley, B., 2008. Glacial geomorphology of the central Arctic Ocean: the Chukchi Borderland and the Lomonosov Ridge. Earth Surface Processes and Landforms, 33, 526−545.

Jakobsson, M., Nilsson, J., O’Regan, M., Backman, J., Löwemark, L., Dowdeswell, J. A., Mayer, L., Polyak, L., Colleoni, F., Anderson, L. G., Björk, G., Darby, D. A., Eriksson, B., Hanslik, D., Hell, B., Marcussen, C., Sellén, E., & Wallin, Å., 2010. An Arctic Ocean ice shelf during MIS 6 constrained by new geophysical and geological data. Quaternary Science Reviews, 29, 3505−3517.

Jakobsson, M., Andreassen, K., Bjarnadottir, L. R., Dove, D., Dow- deswell, J. A., England, J. H., Funder, S., Hogan, K., Ingolfsson, O., Jennings, A., Larsen, N. K., Kirchner, N., Landvik, J. Y., Mayer, L., Mikkelsen, N., Moller, P., Niessen, F., Nilsson, J., O’Regan, M., Polyak, L., Nørgaard-Pedersen, N. & Stein, R. 2014. Arctic Ocean glacial history. Quaternary Science Reviews, 92, 40−67.

Lisiecki, L. E., & Lisiecki, P. A., 2002. Application of dynamic programming to the correlation of paleoclimate records. Paleoceanography and Paleoclimatology, 17, doi:10.1029/2001PA000733.

Lisiecki, L. E., & Raymo, M. E., 2005. A Pliocene-Pleistocene stack of 57 globally distributed benthic δ18O records. Paleoceanography, 20, doi:10.1029/2004PA001071.

Löwemark, L., O'Regan, M., Hanebuth, T. J. J., & Jakobsson, M., 2012. Late Quaternary spatial and temporal variability in Arctic deep-sea bioturbation and its relation to Mn cycles. Palaeogeography, Palaeoclimatology, Palaeoecology, 365, 192−208.

Löwemark, L., März, C., O'Regan, M., & Gyllencreutz, R., 2014. Arctic Ocean Mn-stratigraphy: genesis, synthesis and inter-basin correlation. Quaternary Science Reviews, 92, 97−111.

Macdonald, R. W., & Gobeil, C., 2012. Manganese sources and sinks in the Arctic Ocean with reference to periodic enrichments in basin sediments. Aquatic Geochemistry, 18, 565−591.

Matthiessen, J., Niessen, F., Stein, R., & Naafs, B. D. A., 2010. Pleistocene glacial marine sedimentary environments at the eastern Mendeleev Ridge, Arctic Ocean. Polarforschung, 79, 123−137.

März, C., Stratmann, A., Matthießen, J., Meinhardt, A. K., Eckert, S., Schnetger, B., Vogt, C., Stein, R., & Brumsack, H. J., 2011. Manganese-rich brown layers in Arctic Ocean sediments: composition, formation mechanisms, and diagenetic overprint. Geochimica et Cosmochimica Acta, 75, 7668−7687.

Meinhardt, A. K., März, C., Stein, R., & Brumsack, H. J., 2014. Regional variations in sediment geochemistry on a transect across the Mendeleev Ridge (Arctic Ocean). Chemical Geology, 369, 1−11.

Niessen, F., Hong, J. K., Hegewald, A., Matthiessen, J., Stein, R., Kim, H., Kim, S., Jensen, L., Jokat, W., Nam, S. I., & Kang, S. H., 2013. Repeated Pleistocene glaciation of the East Siberian continental margin. Nature Geoscience, 6, 842.

Nowaczyk, N. R., Frederichs, T. W., Kassens, H., Nørgaard-Pedersen, N., Spielhagen, R. F., Stein, R., & Weiel, D., 2001. Sedimentation rates in the Makarov Basin, central Arctic Ocean: A paleomagnetic and rock magnetic approach. Paleoceanography, 16, 368−389.

O'Regan, M., King, J., Backman, J., Jakobsson, M., Pälike, H., Moran, K., Heil, C., Sakamoto, T., Cronin, T. M., & Jordan, R. W., 2008. Constraints on the Pleistocene chronology of sediments from the Lomonosov Ridge. Paleoceanography, 23, doi: 10.1029/2007PA001551.

O'Regan, M., Coxall, H. K., Cronin, T. M., Gyllencreutz, R., Jakobsson, M., Kaboth, S., Löwemark L., Wiers S., & West, G., 2019. Stratigraphic Occurrences of Sub-Polar Planktonic Foraminifera in Pleistocene Sediments on the Lomonosov Ridge, Arctic Ocean. Frontiers in Earth Science, 7, 71.

Park, K., Ohkushi, K. I., Cho, H. G., & Khim, B. K., 2017. Lithostratigraphy and paleoceanography in the Chukchi Rise of the western Arctic Ocean since the last glacial period. Polar Science, 11, 42−53.

Phillips, R. L., & Grantz, A., 2001. Regional variations in provenance and abundance of ice-rafted clasts in Arctic Ocean sediments: implications for the configuration of late Quaternary oceanic and atmospheric circulation in the Arctic. Marine Geology, 172, 91−115.

Polyak, L., & Jakobsson, M., 2011. Quaternary sedimentation in the Arctic Ocean: Recent advances and further challenges. Oceanography, 24, 52−64.

Polyak, L., Curry, W. B., Darby, D. A., Bischof, J., & Cronin, T. M., 2004. Contrasting glacial/interglacial regimes in the western Arctic Ocean as exemplified by a sedimentary record from the Mendeleev Ridge. Palaeogeography, Palaeoclimatology, Palaeoecology, 203, 73−93.

Polyak, L., Darby, D. A., Bischof, J. F., & Jakobsson, M., 2007. Stratigraphic constraints on late Pleistocene glacial erosion and deglaciation of the Chukchi margin, Arctic Ocean. Quaternary Research, 67, 234−245.

Polyak, L., Bischof, J., Ortiz, J. D., Darby, D. A., Channell, J. E., Xuan, C., Kaufman, D. S., Løvlie, R., Schneider, D. A., Eberl, D. D., Adler, R. E., & Council, E. A., 2009. Late Quaternary stratigraphy and sedimentation patterns in the western Arctic Ocean. Global and Planetary Change, 68, 5−17.

Polyak, L., Best, K. M., Crawford, K. A., Council, E. A., & St-Onge, G., 2013. Quaternary history of sea ice in the western Arctic Ocean based on foraminifera. Quaternary Science Reviews, 79, 145−156.

Reimer, P. J., Bard, E., Bayliss, A., Beck, J. W., Blackwell, P. G., Ramsey, C. B., Buck, C. E., Edwards, R. L., Friedrich, M., Grootes, P. M., Guilderson, T. P., Haflidason, H., Hajdas, I., Hatté, C., Heaton, T. J., Hoffman, D. L., Hogg, A. G., Hughen, K. A., Kaiser, K. F., Kromer, B., Manning, S. W., Niu, M., Reimer, R. W., Richards, D. A., Scott, M., Southon, J. R., Staff, R. A., Turney, C. S. M., van der Plicht, J., 2013. IntCal13 and Marine13 radiocarbon age calibration curves 0–50,000 years cal BP. Radiocarbon 55, doi:10.2458/azu_js_rc.55.16947.

Schreck, M., Nam, S. I., Polyak, L., Vogt, C., Kong, G. S., Stein, R., Matthiessen, J., & Niessen, F., 2018. Improved Pleistocene sediment stratigraphy and paleoenvironmental implications for the western Arctic Ocean off the East Siberian and Chukchi margins. Arktos, 4, 21.

Sellén, E., O’Regan, M., & Jakobsson, M., 2010. Spatial and temporal Arctic Ocean depositional regimes: a key to the evolution of ice drift and current patterns. Quaternary

Science Reviews, 29, 3644-3664.

Sorokin, M. Y., Zamansky, Y. Y., Langinen, A. Y., Jackson, H. R., & Macnab, R., 1999. Crustal structure of the Makarov Basin, Arctic Ocean determined by seismic refraction. Earth and Planetary Science Letters, 168, 187−199.

Spielhagen, R. F., Baumann, K. H., Erlenkeuser, H., Nowaczyk, N. R., Nørgaard-Pedersen, N., Vogt, C., & Weiel, D., 2004. Arctic Ocean deep-sea record of northern Eurasian ice sheet history. Quaternary Science Reviews, 23, 1455−1483.

Stein, R., 2008. Arctic Ocean sediments: processes, proxies, and paleoenvironment (Vol. 2). Elsevier.

Stein, R., Matthiessen, J., Niessen, F., Krylov, A., Nam, S. I., & Bazhenova, E., 2010a. Towards a better (litho-) stratigraphy and reconstruction of Quaternary paleoenvironment in the Amerasian Basin (Arctic Ocean). Polarforschung, 79, 97−121.

Stein, R., Matthiessen, J., & Niessen, F., 2010b. Re-coring at Ice Island T3 site of key core FL-224 (Nautilus Basin, Amerasian Arctic): sediment characteristics and stratigraphic framework. Polarforschung, 79, 81−96.

Vogt, C., 1997. Regional and temporal variations of mineral assemblages in Arctic Ocean sediments as climatic indicator during glacial/interglacial changes. Reports on Polar Research, 251, 309.

Wang, R., Polyak, L., Xiao, W., Wu, L., Zhang, T., Sun, Y., & Xu, X., 2018. Late-Middle Quaternary lithostratigraphy and sedimentation patterns on the Alpha Ridge, central Arctic Ocean: Implications for Arctic climate variability on orbital time scales. Quaternary Science Reviews, 181, 93−108.

Xuan, C., Channell, J. E., Polyak, L., & Darby, D. A., 2012. Paleomagnetism of Quaternary sediments from Lomonosov Ridge and Yermak Plateau: implications for age models in the Arctic Ocean. Quaternary Science Reviews, 32, 48−63.

Table captions

Table 1. List of AMS ^{14}C dating for ARA03B-41GC02 and 41MUC. No ΔR was applied for calibration using CALIB 7.10.

Table 2. An overview of the age models based on visual and computational correlations. ln Mn/Al = natural logarithmic Mn/Al ratio, LR04 = LR04 benthic oxygen isotopic stack (Lisiecki and Raymo, 2005).

Figure captions

Fig. 1. A map showing the study area with the locations of core ARA03B-41GC02 (41GC) and reference cores HLY0503-08JPC (08JPC; Adler et al., 2009), 92/12-1pc (Jakobsson et al., 2000), ACEX (O'Regan et al., 2008), PS72/392-5 (392-5; Stein et al., 2010b), and ARC4-BN05 (BN05; Dong et al., 2017) marked as yellow and green circles, respectively. Glacier limits (white dashed line) during the LGM are modified from Ehlers and Gibbard (2004), Svendsen et al. (2004), and Jakobsson et al. (2013). White arrows correspond to the surface currents of the Arctic Ocean. BG = Beaufort Gyre; TPD = Transpolar Drift; CB = Chukchi Borderland; MR = Mendeleev Ridge; AR = Alpha Ridge; LR = Lomonosov Ridge; GR = Gakkel Ridge.

Fig. 2. Profiles of color reflectance (L* and a*), XRF-elemental ratio (Mn/Al and Ca/Al), physical properties (magnetic susceptibility (MS) and wet bulk density (WBD)), and sand fraction (>63 μm %) with the core surface image of core ARA03B-41GC02. Brown layers are indicated as B1 to B31 with brown shades. Pinkish shading indicates pink-white (PW)

layer.

Fig. 3. Visual correlation between cores ARA03B-41GC02 and ARC4-BN05 (Dong et al., 2017) mainly based on the presence of brown layers and lithological features including color reflectance (L*), sand fraction, and PW layer.

Fig. 4. Visual correlation between core ARA03B-41GC02 and LR04 applied beyond the MIS 5/6 boundary. Brown shades indicate brown layers (left panel) and interglacial periods (right panel).

Fig. 5. Plots of computational correlations between ln Mn/Al of the core ARA03B-41GC02 and LR04.

Fig. 6. Age-depth plots of visual correlations (VC01-VC02) and computational correlations (MA01-MA05) for core ARA03B-41GC02.

Fig. 7. Plots of Ca/Al ratios of core ARA03B-41GC02 using age models MA01-05. Blue shades indicate glacial periods.

Supplementary information

Fig. S1. Visual correlation between cores ARA03B-41GC02 and HLY0503-08JPC (Adler et al., 2009) based on lithological features including color reflectance (L*), WBD, and sand fraction.

Fig. S2. Plots of ln Mn/Al of core ARA03B-41GC02 versus LR04 based on the age models derived from the visual correlations (VC01, VC02, and the combination of VC01 and VC02, i.e., VC01-02).

Fig. S3. Computational correlation (WBD01) based on WBD data of core 41GC with those of ACEX (O'Regan et al., 2008) and a plot of ln Mn/Al of core ARA03B-41GC02 versus LR04 based on age model WBD01. Please note that the WBD01 match started from a core depth of ~160 cm corresponding to MIS 5.5 and not from the top of the core.

Table S4. Correlation coefficients (spearman's r^2) among normalized WBD and grain size parameters. Please note that the sand fraction is weight percent for the bulk weight while the other grain size parameters for the mud fraction are volume percent.

Table S5. Age-depth tie points at the Marine Isotope Stage (MIS) boundary for ARA03B-41GC derived from VC02 (Figs. 4 and 6).

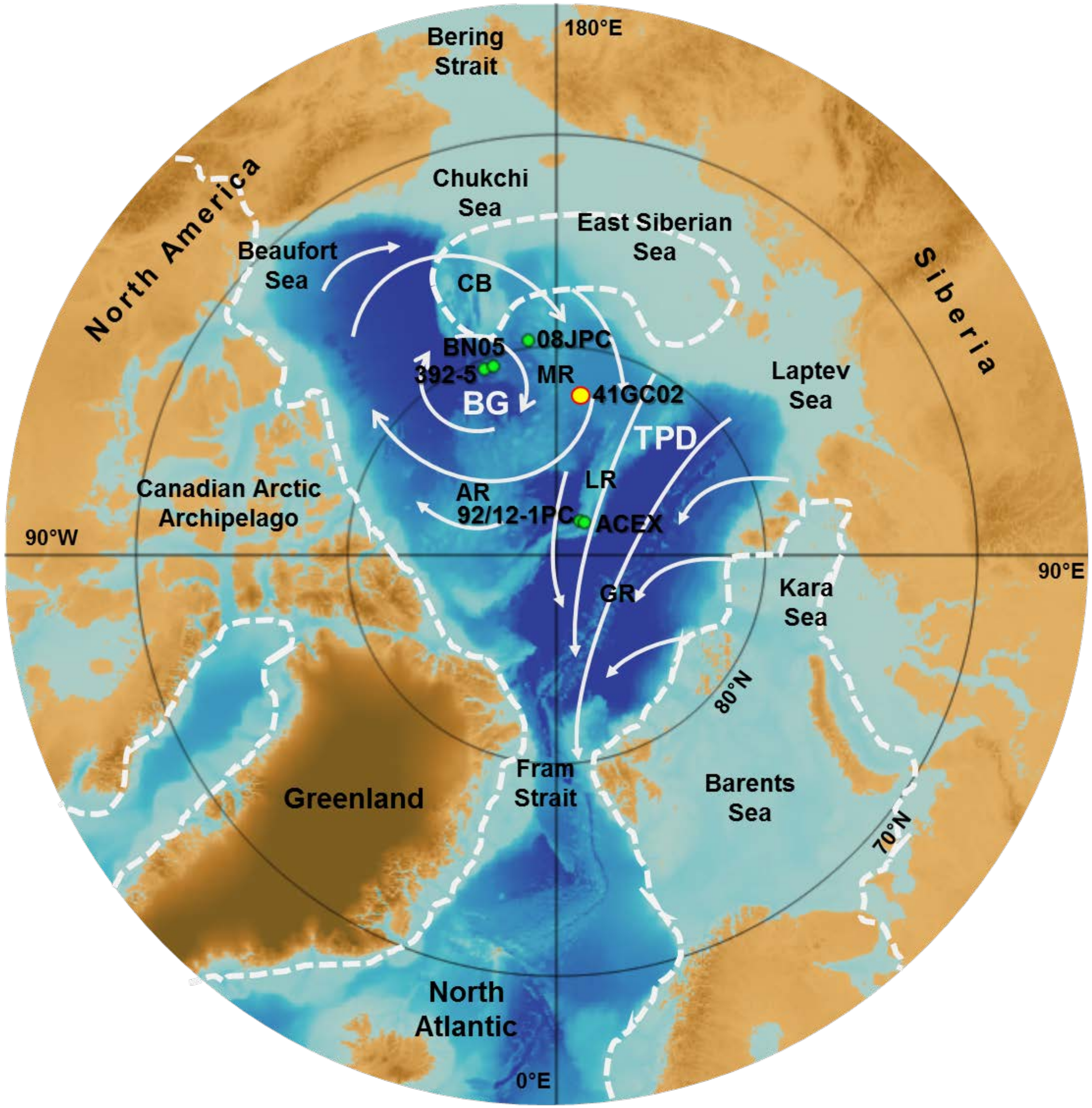
Bering Strait
180°E
North America
Chukchi Sea
East Siberian Sea
Siberia
Beaufort Sea
CB
08JPC
BN05
392-5
MR
41GC02
BG
Laptev Sea
TPD
LR
Canadian Arctic Archipelago
AR
92/12-1PC
ACEX
90°W
90°E
GR
Kara Sea
80°N
Fram Strait
Barents Sea
Greenland
70°N
North Atlantic
0°E

Fig. 1

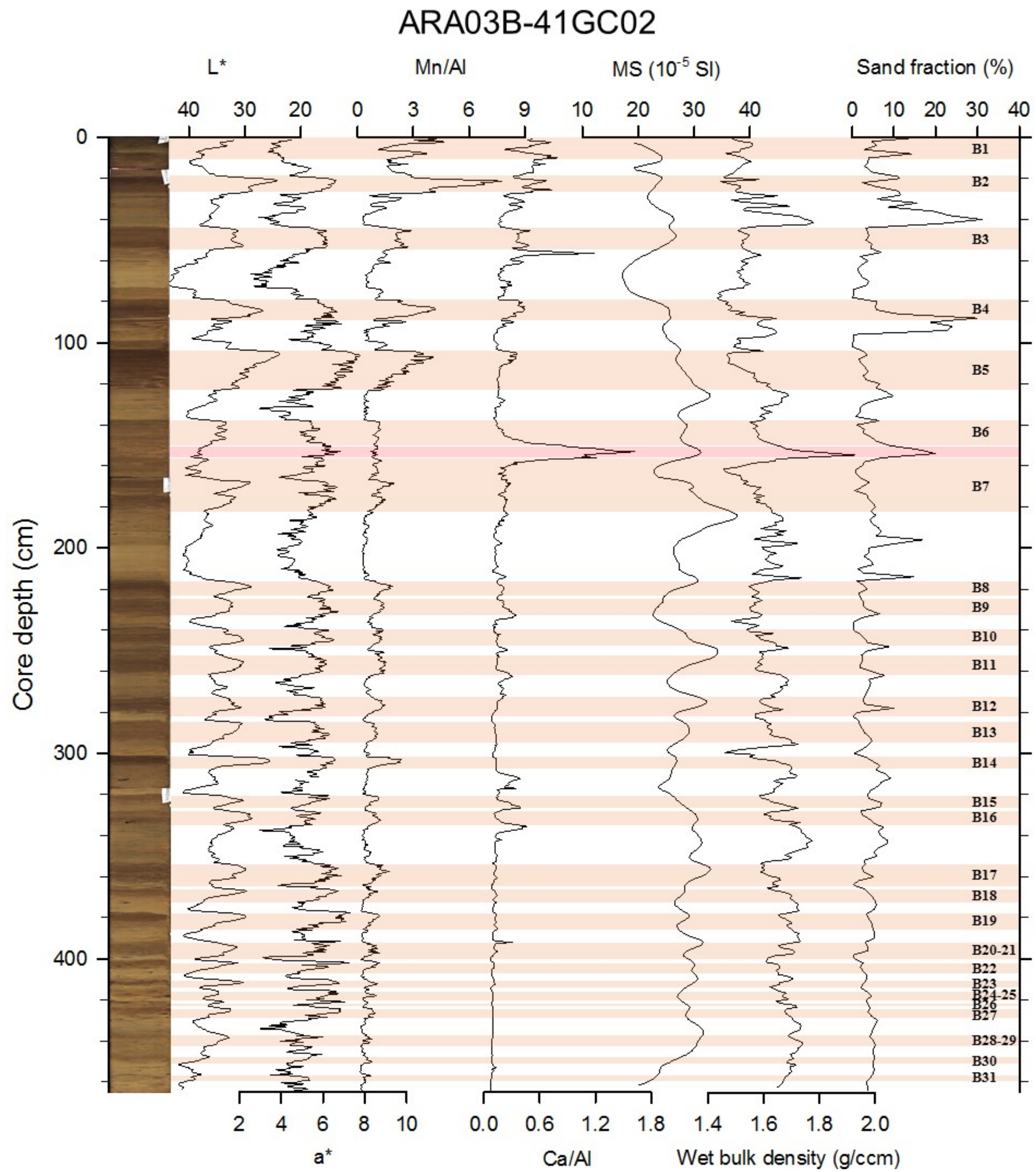
ARA03B-41GC02
L*
Mn/Al
MS (10^{-5} SI)
Sand fraction (%)
Core depth (cm)
a*
Ca/Al
Wet bulk density (g/ccm)
B1
B2
B3
B4
B5
B6
B7
B8
B9
B10
B11
B12
B13
B14
B15
B16
B17
B18
B19
B20-21
B22
B23
B24-25
B26
B27
B28-29
B30
B31

Fig. 2

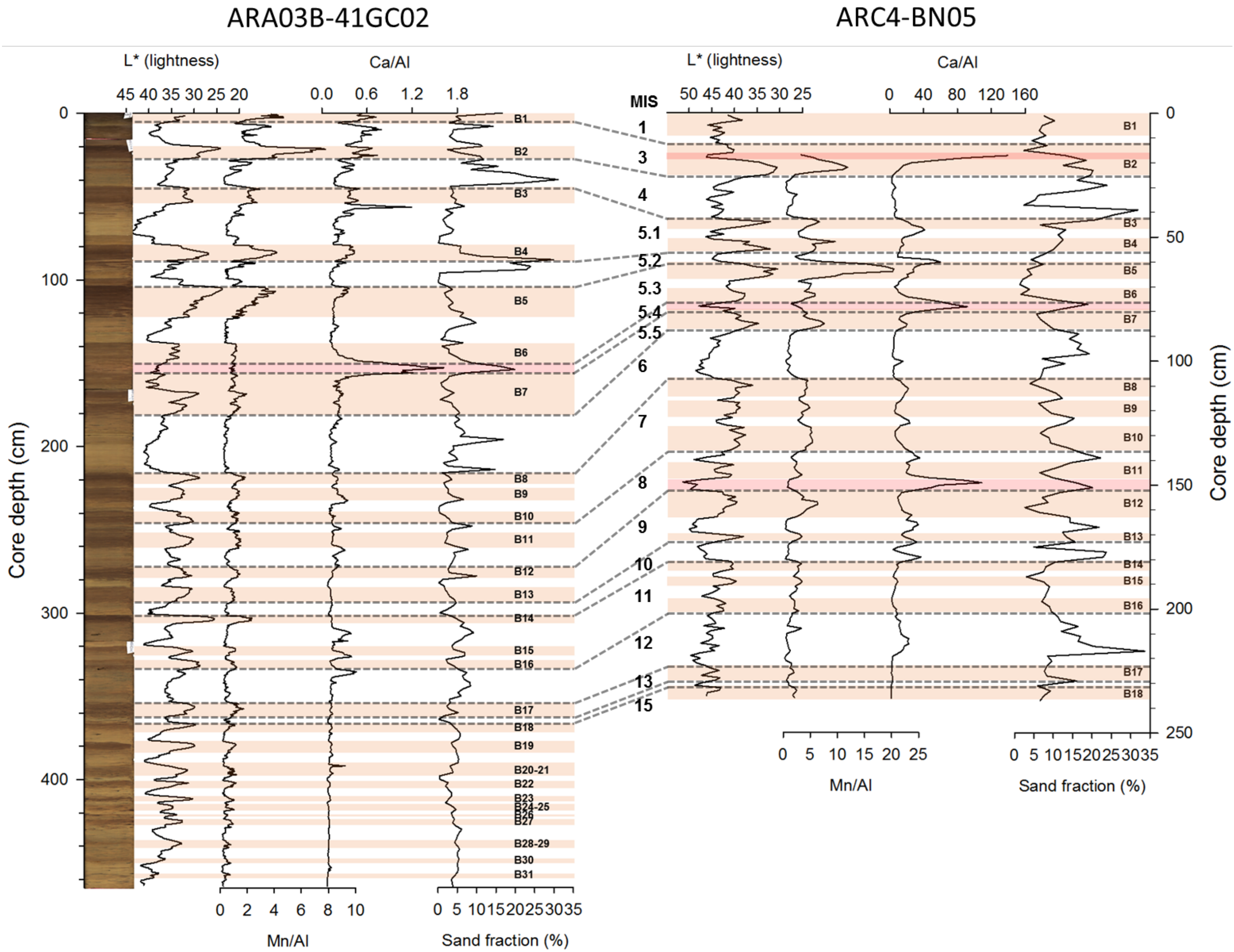
ARA03B-41GC02
ARC4-BN05
L* (lightness)
Ca/Al
Mn/Al
Sand fraction (%)
Core depth (cm)
MIS

Fig. 3

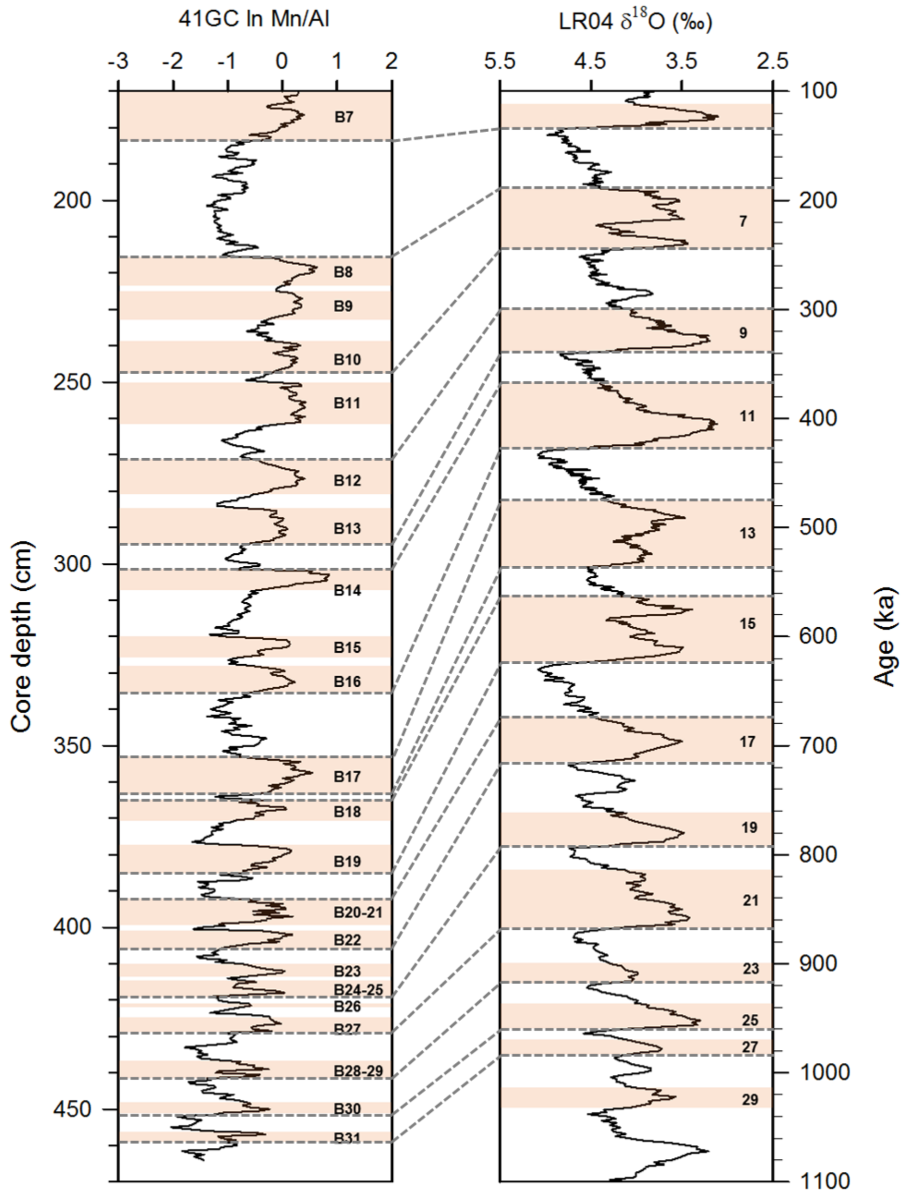

41GC ln Mn/Al
LR04 δ18O (‰)
Core depth (cm)
Age (ka)
-3
-2
-1
0
1
2
5.5
4.5
3.5
2.5
200
250
300
350
400
450
100
200
300
400
500
600
700
800
900
1000
1100
B7
B8
B9
B10
B11
B12
B13
B14
B15
B16
B17
B18
B19
B20-21
B22
B23
B24-25
B26
B27
B28-29
B30
B31
7
9
11
13
15
17
19
21
23
25
27
29

Fig. 4

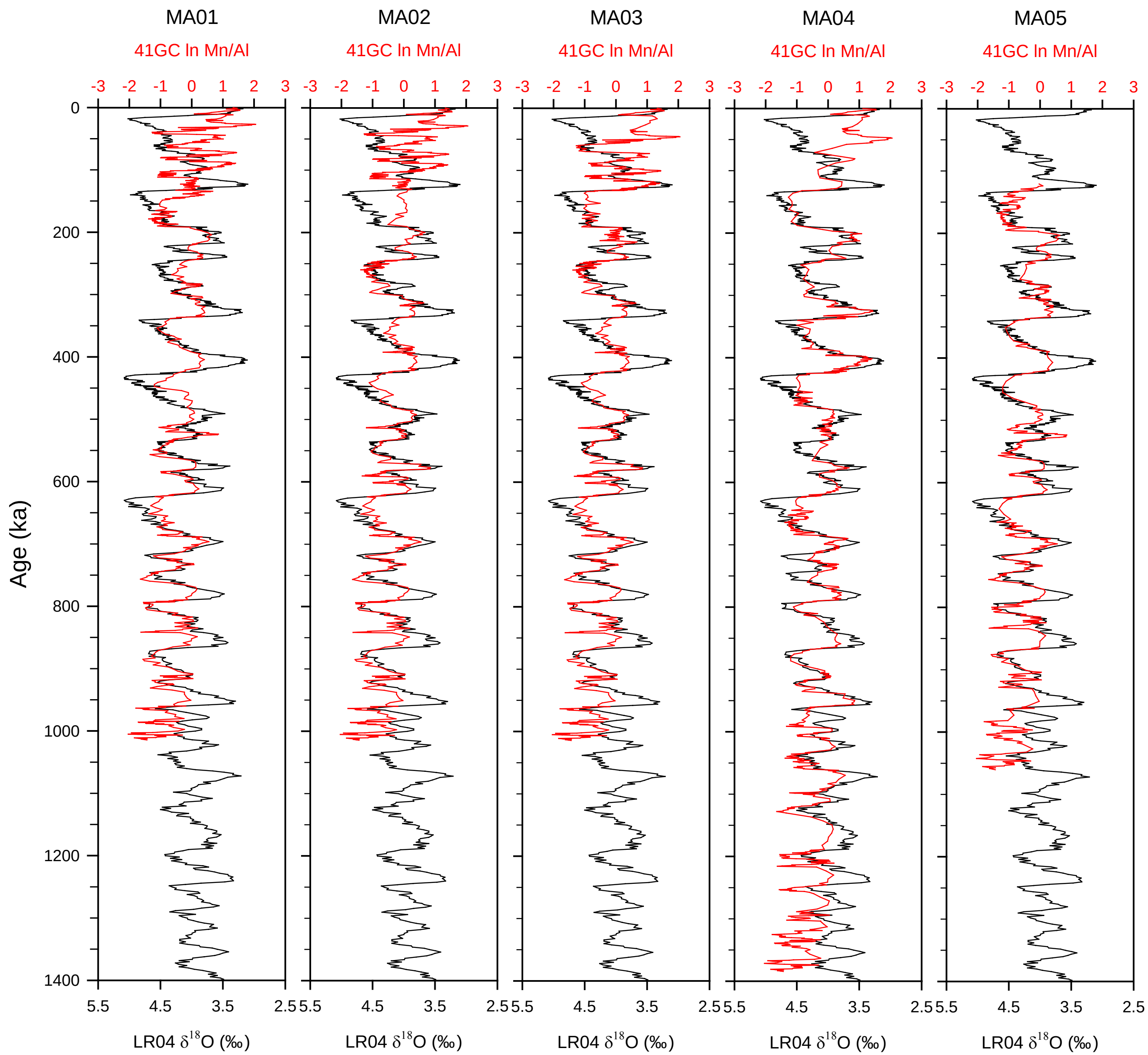

MA01
MA02
MA03
MA04
MA05
41GC ln Mn/Al
41GC ln Mn/Al
41GC ln Mn/Al
41GC ln Mn/Al
41GC ln Mn/Al
-3 -2 -1 0 1 2 3
Age (ka)
0
200
400
600
800
1000
1200
1400
5.5 4.5 3.5 2.5
LR04 δ18O (‰)
LR04 δ18O (‰)
LR04 δ18O (‰)
LR04 δ18O (‰)
LR04 δ18O (‰)

Fig. 5

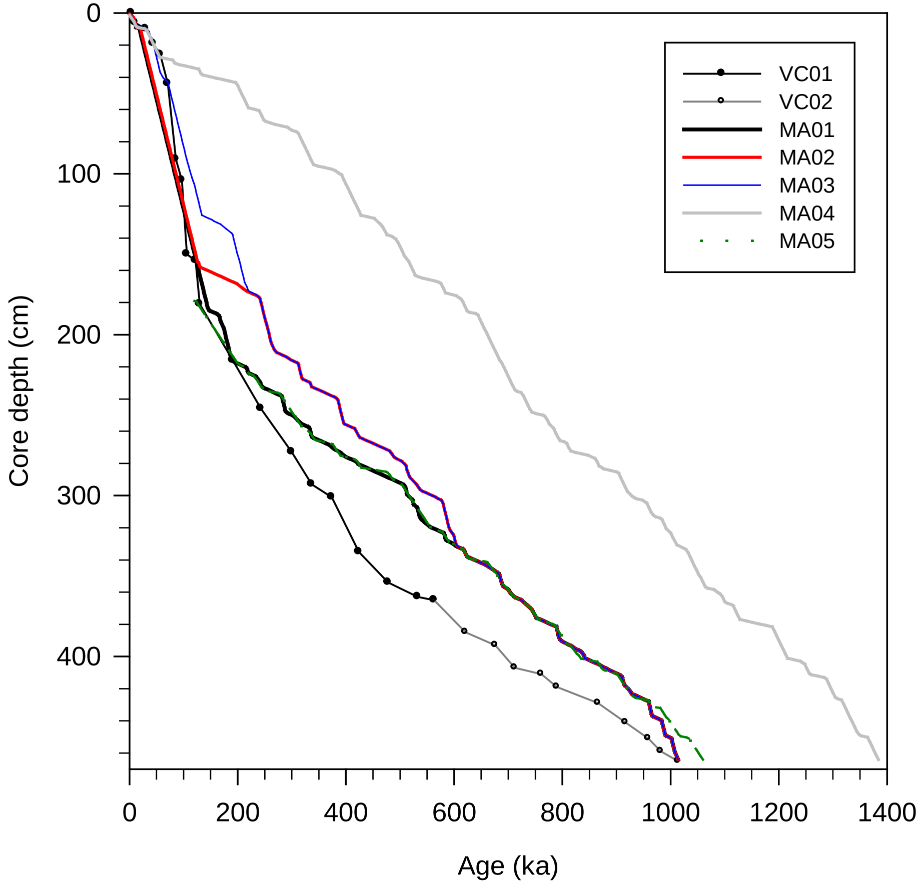

Core depth (cm)
Age (ka)
0
100
200
300
400
0
200
400
600
800
1000
1200
1400
VC01
VC02
MA01
MA02
MA03
MA04
MA05

Fig. 6

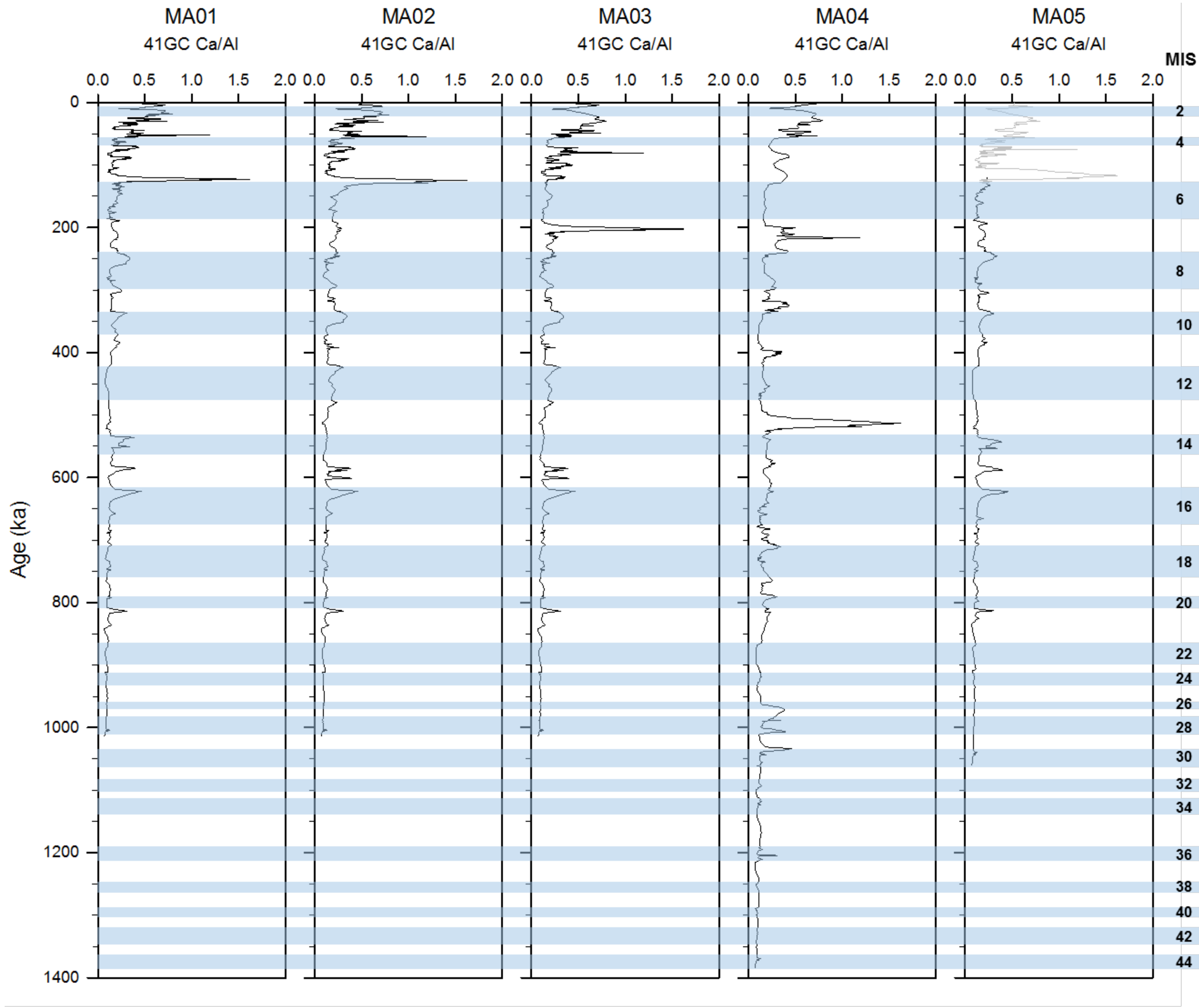

MA01
41GC Ca/Al
MA02
41GC Ca/Al
MA03
41GC Ca/Al
MA04
41GC Ca/Al
MA05
41GC Ca/Al
MIS
0.0 0.5 1.0 1.5 2.0
Age (ka)
0
200
400
600
800
1000
1200
1400
2
4
6
8
10
12
14
16
18
20
22
24
26
28
30
32
34
36
38
40
42
44

Fig. 7

Table 1

Core	Core depth (cm)	Material	Uncorrected AMS ^{14}C age (yr)	1σ (±)	Calibrated age (cal. yr BP)	1σ (±)	Lab ID
41MUC	0-1	*N. pachyderma*	3470	30	3369	28	463639
41GC	0-1	*N. pachyderma*	3910	30	3883	48	463637
41GC	6-7	*N. pachyderma*	10230	30	11212	38	444525
41GC	10-11	*N. pachyderma*	30210	180	33915	154	444526
41GC	19-20	*N. pachyderma*	40670	580	43844	520	463638

Table 2

Age model	Method	Signal of ARA03B 41GC02	Target data	Age constraints	Target core depth	End point limit
VC01	Manual correlation	Brown layer	Brown layer (ARC4-BN05)	AMS ^{14}C ages, PW2 (MIS 5.4), and MIS boundaries (MIS 1/2 to 14/15)	Top to ~370 cm	-
VC02	Manual correlation	Brown layer	LR04	MIS boundaries (MIS 5/6 to 27/28)	~130 cm to bottom	-
MA01	Match program	ln Mn/Al	LR04	AMS ^{14}C ages, PW2 (MIS 5.4), and MIS 5/6 and 6/7 boundaries	Top to bottom	1014 ka
MA02	Match program	ln Mn/Al	LR04	AMS ^{14}C ages and PW2 (MIS 5.4)	Top to bottom	1014 ka
MA03	Match program	ln Mn/Al	LR04	AMS ^{14}C ages	Top to bottom	1014 ka
MA04	Match program	ln Mn/Al	LR04	AMS ^{14}C ages	Top to bottom	No limit
MA05	Match program	ln Mn/Al	LR04	MIS 5/6 and 6/7 boundaries	160 cm to bottom	No limit
WBD01	Match program	Wet bulk density (WBD)	ACEX WBD	MIS 5/6 and 6/7 boundaries	160 cm to bottom	No limit

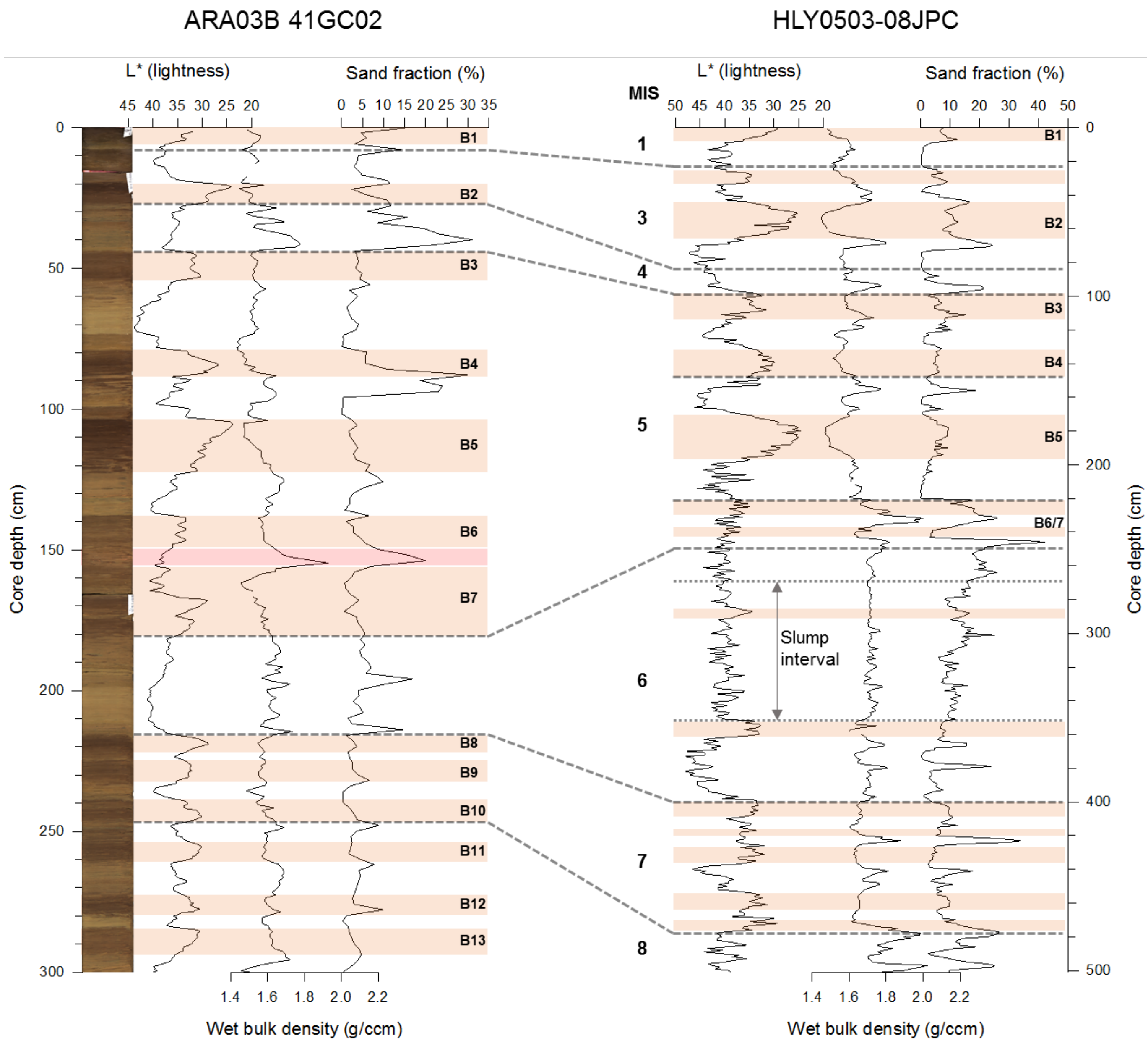

ARA03B 41GC02
HLY0503-08JPC
L* (lightness)
Sand fraction (%)
MIS
Core depth (cm)
Wet bulk density (g/ccm)
B1
B2
B3
B4
B5
B6
B7
B8
B9
B10
B11
B12
B13
B6/7
Slump interval

Fig. S1

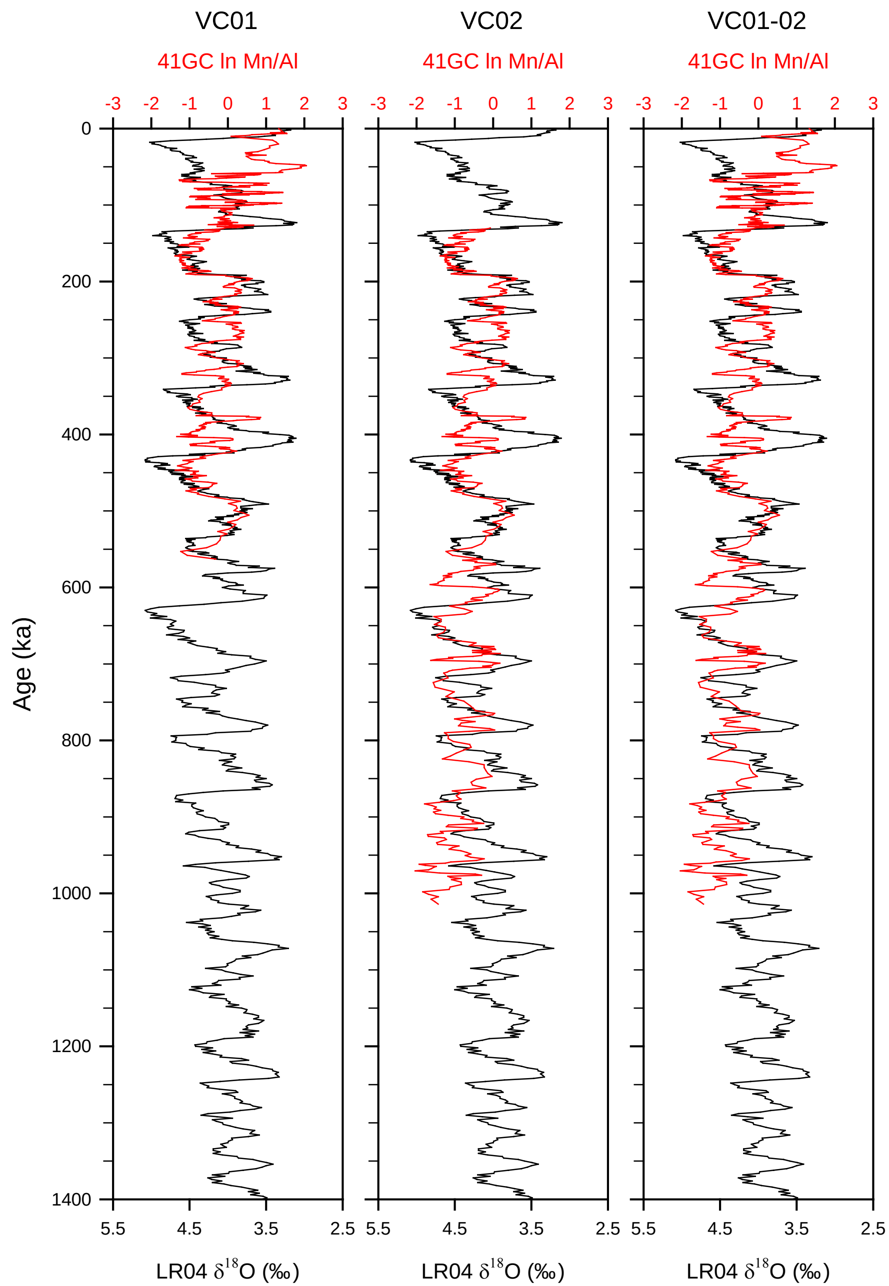
VC01
VC02
VC01-02
41GC ln Mn/Al
41GC ln Mn/Al
41GC ln Mn/Al
-3 -2 -1 0 1 2 3
0
200
400
600
800
1000
1200
1400
Age (ka)
5.5 4.5 3.5 2.5
LR04 δ18O (‰)
LR04 δ18O (‰)
LR04 δ18O (‰)

Fig. S2

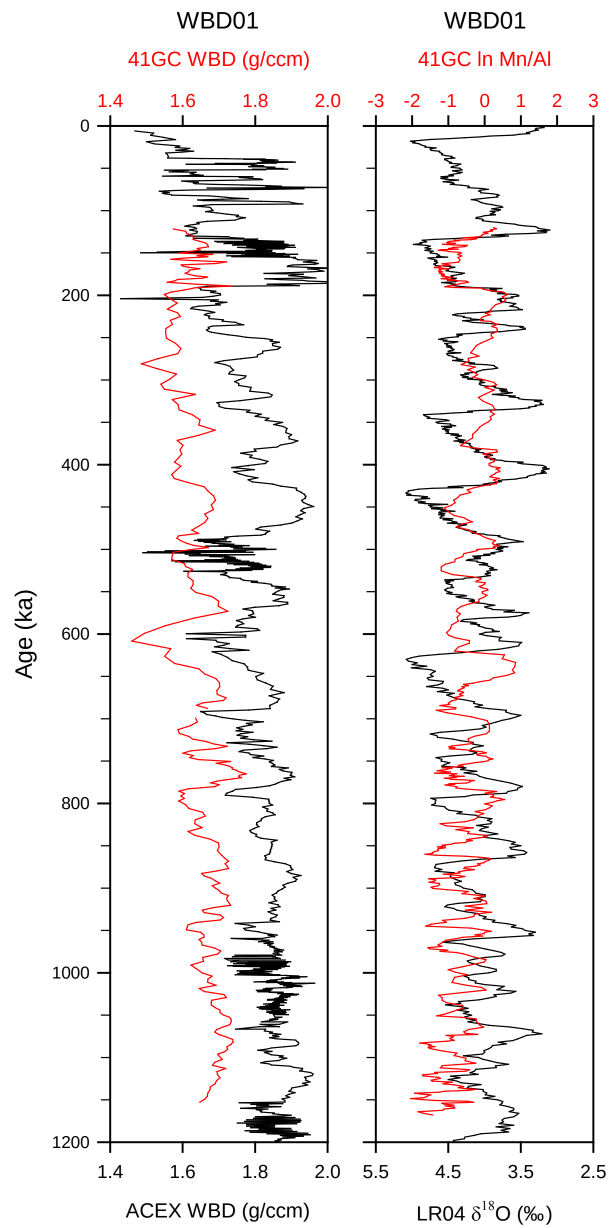
WBD01
41GC WBD (g/ccm)
WBD01
41GC ln Mn/Al
1.4
1.6
1.8
2.0
-3
-2
-1
0
1
2
3
0
200
400
600
800
1000
1200
Age (ka)
1.4
1.6
1.8
2.0
5.5
4.5
3.5
2.5
ACEX WBD (g/ccm)
LR04 δ18O (‰)

Fig. S3

	WBD (g/ccm)	Sand fraction (> 63 μm)	Silt (2–63 μm)	Coarse silt (20–63 μm)	Medium silt (6.3–20 μm)	Fine silt (2–6.3 μm)	Clay (< 2 μm)
WBD	–						
Sand fraction	0.42	–					
Silt	0.71	-0.04	–				
Coarse silt	0.61	0.54	0.32	–			
Medium silt	0.54	-0.01	0.52	0.43	–		
Fine silt	-0.45	-0.48	-0.21	-0.83	-0.25	–	
Clay	-0.58	-0.24	-0.41	-0.66	-0.83	0.28	–

Table S4

MIS boundary	Age (ka)	Core depth (cm)
5/6	130	181
6/7	191	216
7/8	243	246
8/9	300	273
9/10	337	293
10/11	374	301
11/12	424	335
12/13	478	354
13/14	533	363
14/15	563	365
15/16	621	385
16/17	676	392
17/18	712	407
18/19	761	415
19/20	790	419
20/21	814	421
21/22	866	429
22/23	900	438
23/24	917	441
24/25	936	448
25/26	959	451
26/27	970	456
27/28	982	459

Table S5

Table captions

- Table 1. List of AMS ^{14}C dating for ARA03B-41GC02 and 41MUC. No ΔR was applied for calibration using CALIB 7.10.
- Table 2. An overview of the age models based on visual and computational correlations. ln Mn/Al = natural logarithmic Mn/Al ratio, LR04 = LR04 benthic oxygen isotopic stack (Lisiecki and Raymo, 2005).

Figure captions

- Fig. 1. A map showing the study area with the locations of core ARA03B-41GC02 (41GC) and reference cores HLY0503-08JPC (08JPC; Adler et al., 2009), 92/12-1pc (Jakobsson et al., 2000), ACEX (O'Regan et al., 2008), PS72/392-5 (392-5; Stein et al., 2010b), and ARC4-BN05 (BN05; Dong et al., 2017) marked as yellow and green circles, respectively. Glacier limits (white dashed line) during the LGM are modified from Ehlers and Gibbard (2004), Svendsen et al. (2004), and Jakobsson et al. (2013). White arrows correspond to the surface currents of the Arctic Ocean. BG = Beaufort Gyre; TPD = Transpolar Drift; CB = Chukchi Borderland; MR = Mendeleev Ridge; AR = Alpha Ridge; LR = Lomonosov Ridge; GR = Gakkel Ridge.
- Fig. 2. Profiles of color reflectance (L* and a*), XRF-elemental ratio (Mn/Al and Ca/Al), physical properties (magnetic susceptibility (MS) and wet bulk density (WBD)), and sand fraction (>63 μm %) with the core surface image of core ARA03B-41GC02. Brown layers are indicated as B1 to B31 with brown shades. Pinkish shading indicates pink-white (PW) layer.
- Fig. 3. Visual correlation between cores ARA03B-41GC02 and ARC4-BN05 (Dong et al., 2017) mainly based on the presence of brown layers and lithological features including color reflectance (L*), sand fraction, and PW layer.
- Fig. 4. Visual correlation between core ARA03B-41GC02 and LR04 applied beyond the MIS 5/6 boundary. Brown shades indicate brown layers (left panel) and interglacial periods (right panel).
- Fig. 5. Plots of computational correlations between ln Mn/Al of the core ARA03B-41GC02 and LR04.
- Fig. 6. Age-depth plots of visual correlations (VC01-VC02) and computational correlations (MA01-MA05) for core ARA03B-41GC02.
- Fig. 7. Plots of Ca/Al ratios of core ARA03B-41GC02 using age models MA01-05. Blue shades indicate glacial periods.

Supplementary information

- Fig. S1. Visual correlation between cores ARA03B-41GC02 and HLY0503-08JPC (Adler et al., 2009) based on lithological features including color reflectance (L*), WBD, and sand fraction.
- Fig. S2. Plots of ln Mn/Al of core ARA03B-41GC02 versus LR04 based on the age models derived from the visual correlations (VC01, VC02, and the combination of VC01 and VC02, i.e., VC01-02).
- Fig. S3. Computational correlation (WBD01) based on WBD data of core 41GC with those of ACEX (O'Regan et al., 2008) and a plot of ln Mn/Al of core ARA03B-41GC02 versus LR04 based on age model WBD01. Please note that the WBD01 match started from a core depth of ~160 cm corresponding to MIS 5.5 and not from the top of the core.
- Table S4. Correlation coefficients (spearman's r^2) among normalized WBD and grain size parameters. Please note that the sand fraction is weight percent for the bulk weight while the other grain size parameters for the mud fraction are volume percent.
- Table S5. Age-depth tie points at the Marine Isotope Stage (MIS) boundary for ARA03B-41GC derived from VC02 (Figs. 4 and 6).

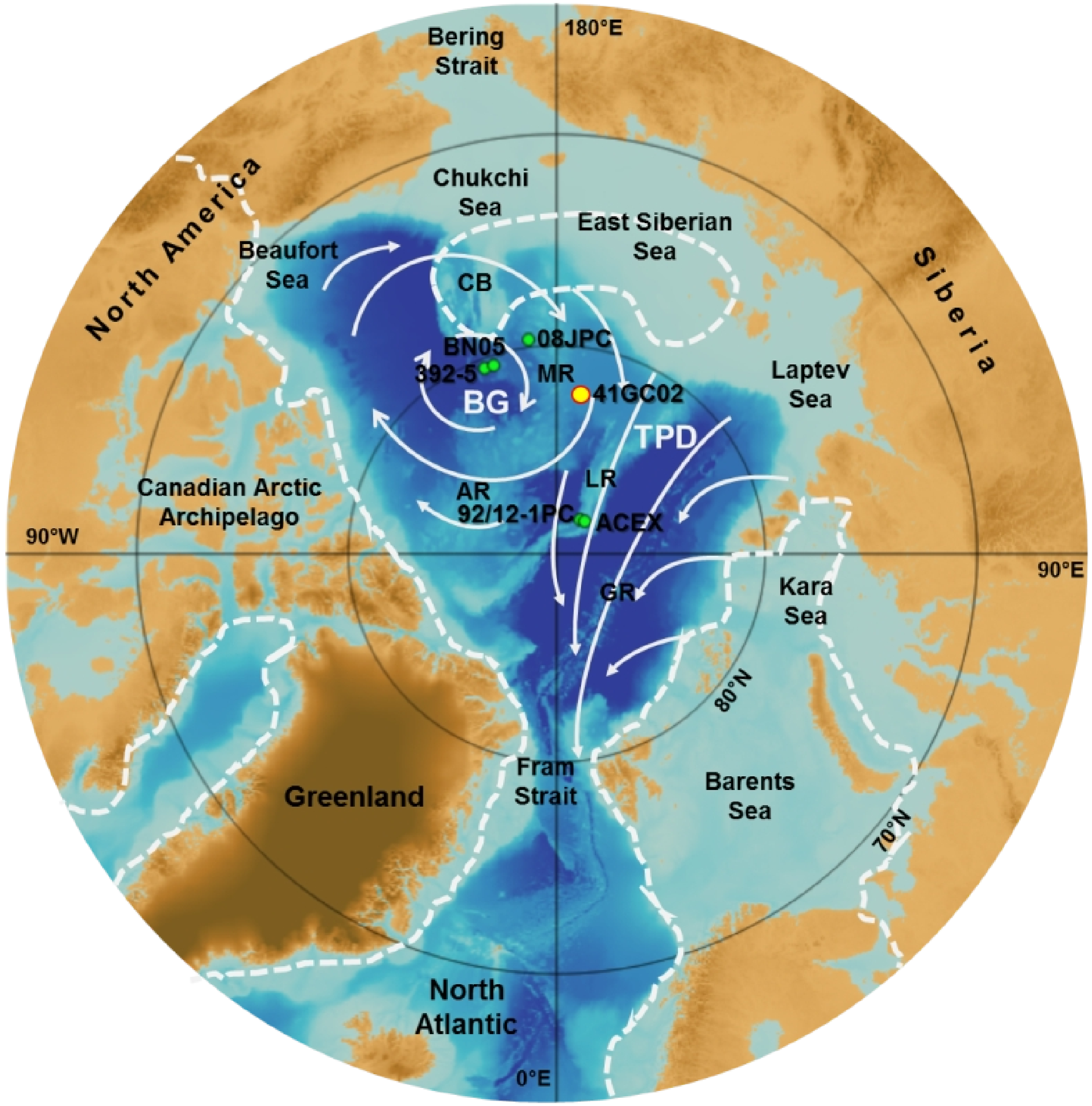

Bering Strait
180°E
Chukchi Sea
East Siberian Sea
North America
Siberia
Beaufort Sea
CB
08JPC
BN05
392-5
MR
41GC02
BG
Laptev Sea
TPD
LR
Canadian Arctic Archipelago
AR
92/12-1PC
ACEX
90°W
90°E
GR
Kara Sea
80°N
Fram Strait
Barents Sea
Greenland
70°N
North Atlantic
0°E

Fig. 1

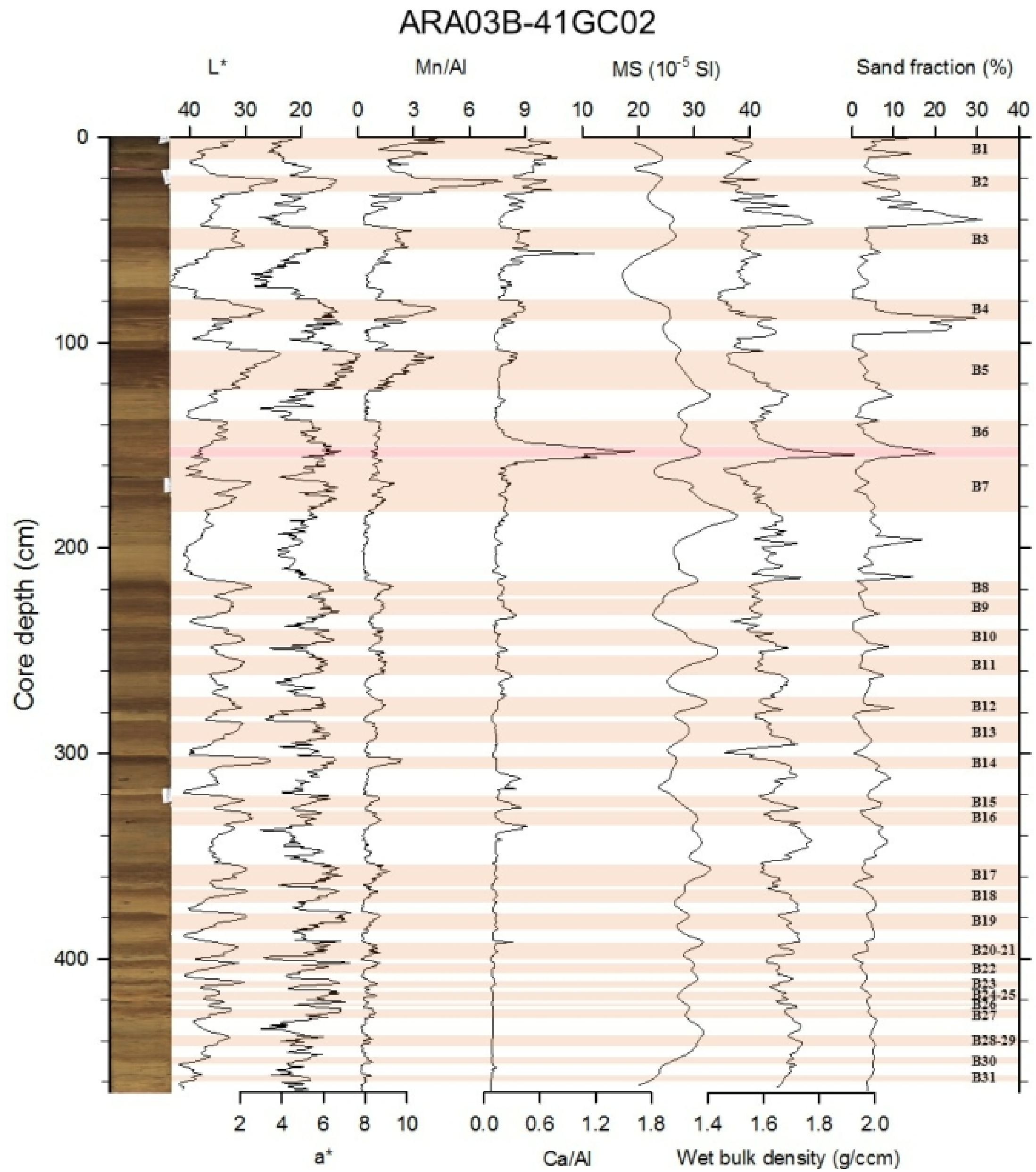
ARA03B-41GC02
L*
Mn/Al
MS (10^{-5} SI)
Sand fraction (%)
Core depth (cm)
a*
Ca/Al
Wet bulk density (g/ccm)
B1
B2
B3
B4
B5
B6
B7
B8
B9
B10
B11
B12
B13
B14
B15
B16
B17
B18
B19
B20-21
B22
B27
B28-29
B30
B31

Fig. 2

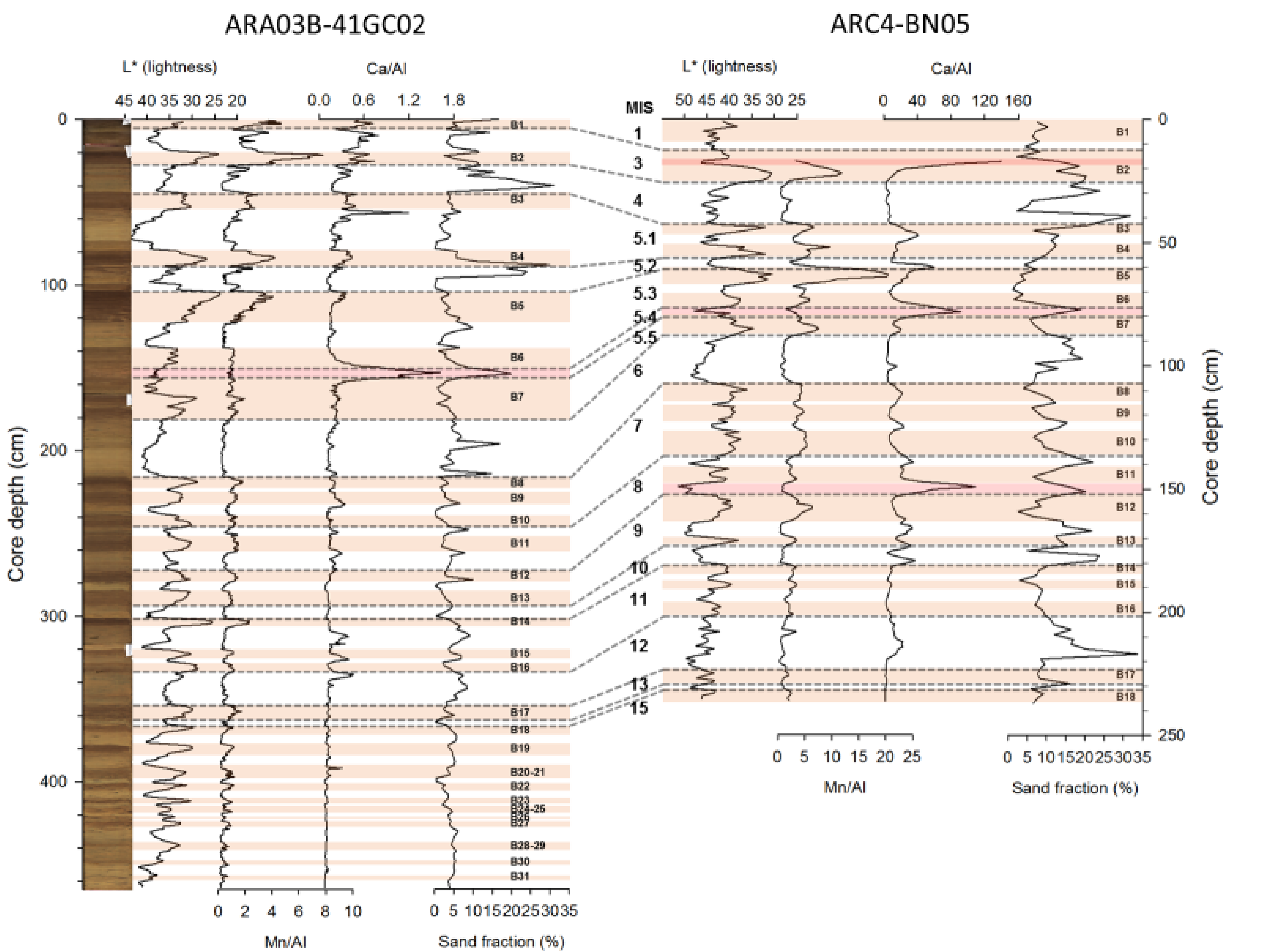

ARA03B-41GC02
ARC4-BN05
L* (lightness)
Ca/Al
MIS
Core depth (cm)
Mn/Al
Sand fraction (%)

Fig. 3

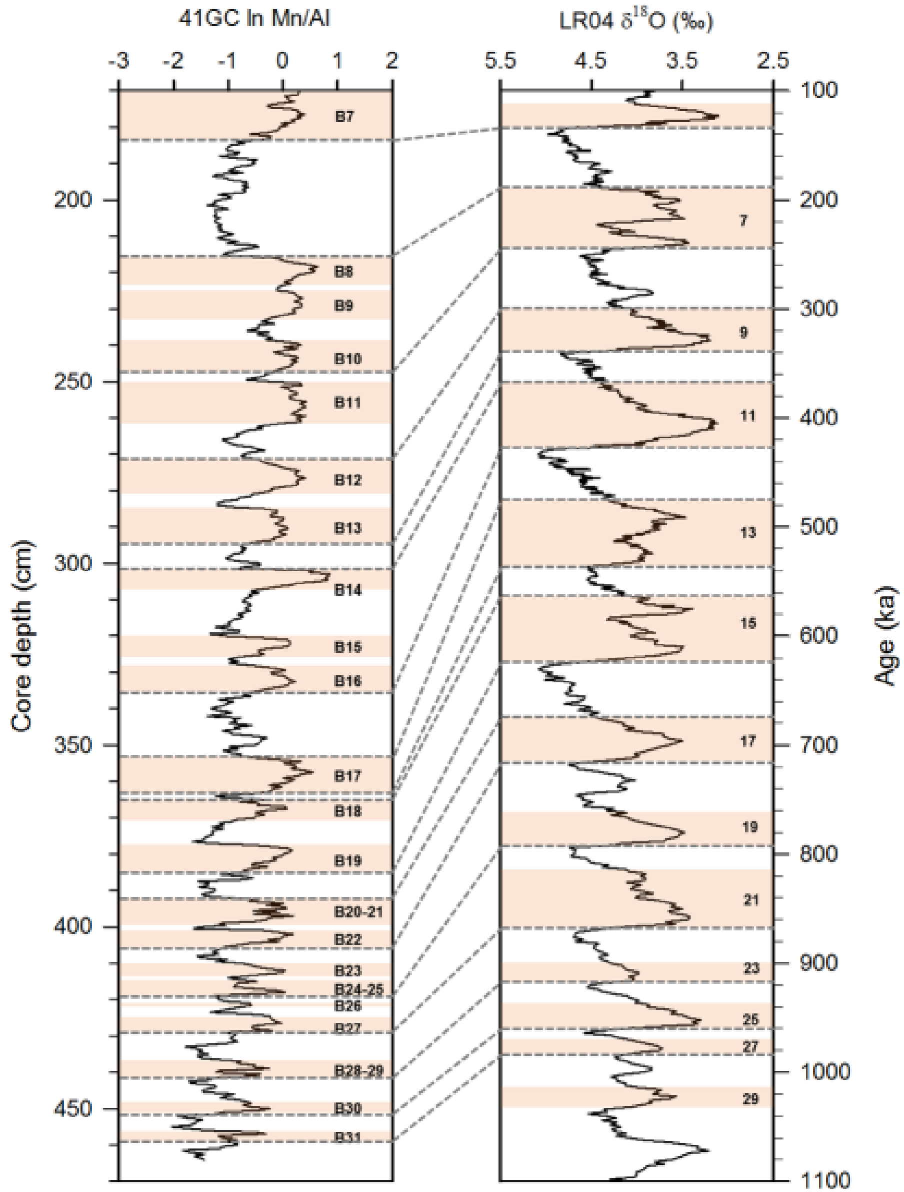
41GC ln Mn/Al
LR04 δ18O (‰)
Core depth (cm)
Age (ka)
-3
-2
-1
0
1
2
5.5
4.5
3.5
2.5
200
250
300
350
400
450
100
200
300
400
500
600
700
800
900
1000
1100
B7
B8
B9
B10
B11
B12
B13
B14
B15
B16
B17
B18
B19
B20-21
B22
B23
B24-25
B26
B27
B28-29
B30
B31
7
9
11
13
15
17
19
21
23
25
27
29

Fig. 4

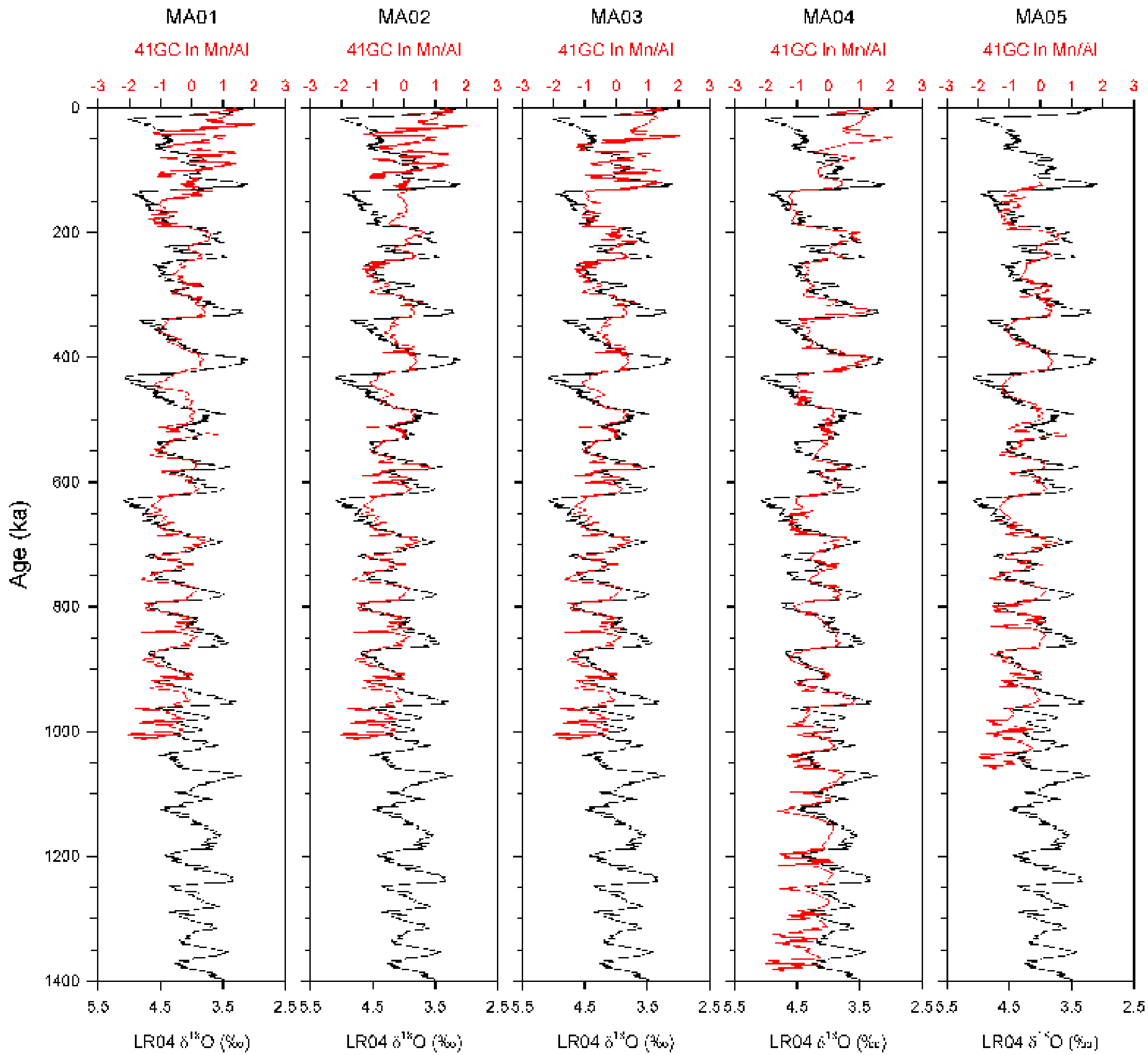
MA01
MA02
MA03
MA04
MA05
41GC ln Mn/Al
-3 -2 -1 0 1 2 3
Age (ka)
0
200
400
600
800
1000
1200
1400
5.5 4.5 3.5 2.5
LR04 δ18O (‰)

Fig. 5

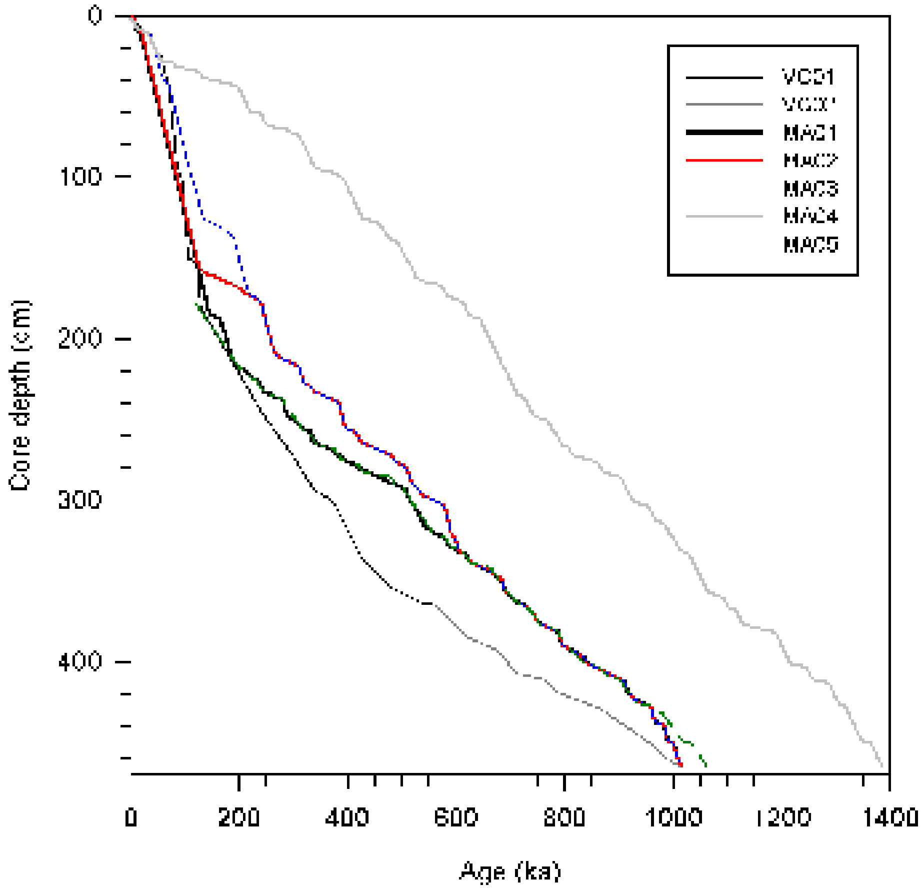

MAC1
MAC2
MAC3
MAC4
MAC5
0
100
200
300
400
Core depth (cm)
0
200
400
600
800
1000
1200
1400
Age (ka)

Fig. 6

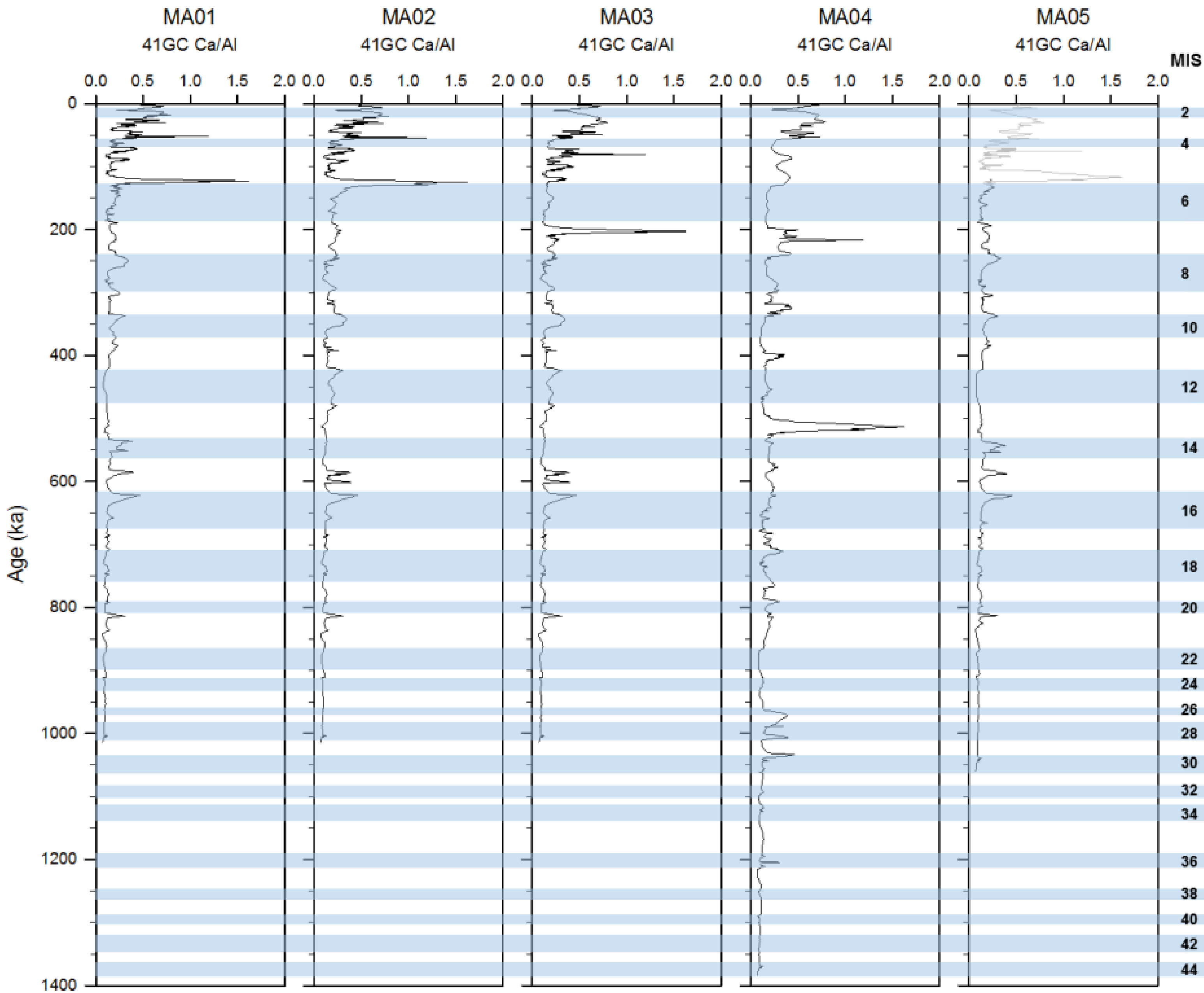
MA01
41GC Ca/Al
MA02
41GC Ca/Al
MA03
41GC Ca/Al
MA04
41GC Ca/Al
MA05
41GC Ca/Al
MIS
0.0 0.5 1.0 1.5 2.0
Age (ka)
0
200
400
600
800
1000
1200
1400
2
4
6
8
10
12
14
16
18
20
22
24
26
28
30
32
34
36
38
40
42
44

Fig. 7

Table 1

Core	Core depth (cm)	Material	Uncorrected AMS ^{14}C age (yr)	1σ (±)	Calibrated age (cal. yr BP)	1σ (±)	Lab ID
41MUC	0-1	*N. pachyderma*	3470	30	3369	28	463639
41GC	0-1	*N. pachyderma*	3910	30	3883	48	463637
41GC	6-7	*N. pachyderma*	10230	30	11212	38	444525
41GC	10-11	*N. pachyderma*	30210	180	33915	154	444526
41GC	19-20	*N. pachyderma*	40670	580	43844	520	463638

Table 2

Age model	Method	Signal of ARA03B 41GC02	Target data	Age constraints	Target core depth	End point limit
VC01	Manual correlation	Brown layer	Brown layer (ARC4-BN05)	AMS ^{14}C ages, PW2 (MIS 5.4), and MIS boundaries (MIS 1/2 to 14/15)	Top to ~370 cm	-
VC02	Manual correlation	Brown layer	LR04	MIS boundaries (MIS 5/6 to 27/28)	~130 cm to bottom	-
MA01	Match program	ln Mn/Al	LR04	AMS ^{14}C ages, PW2 (MIS 5.4), and MIS 5/6 and 6/7 boundaries	Top to bottom	1014 ka
MA02	Match program	ln Mn/Al	LR04	AMS ^{14}C ages and PW2 (MIS 5.4)	Top to bottom	1014 ka
MA03	Match program	ln Mn/Al	LR04	AMS ^{14}C ages	Top to bottom	1014 ka
MA04	Match program	ln Mn/Al	LR04	AMS ^{14}C ages	Top to bottom	No limit
MA05	Match program	ln Mn/Al	LR04	MIS 5/6 and 6/7 boundaries	160 cm to bottom	No limit
WBD01	Match program	Wet bulk density (WBD)	ACEX WBD	MIS 5/6 and 6/7 boundaries	160 cm to bottom	No limit

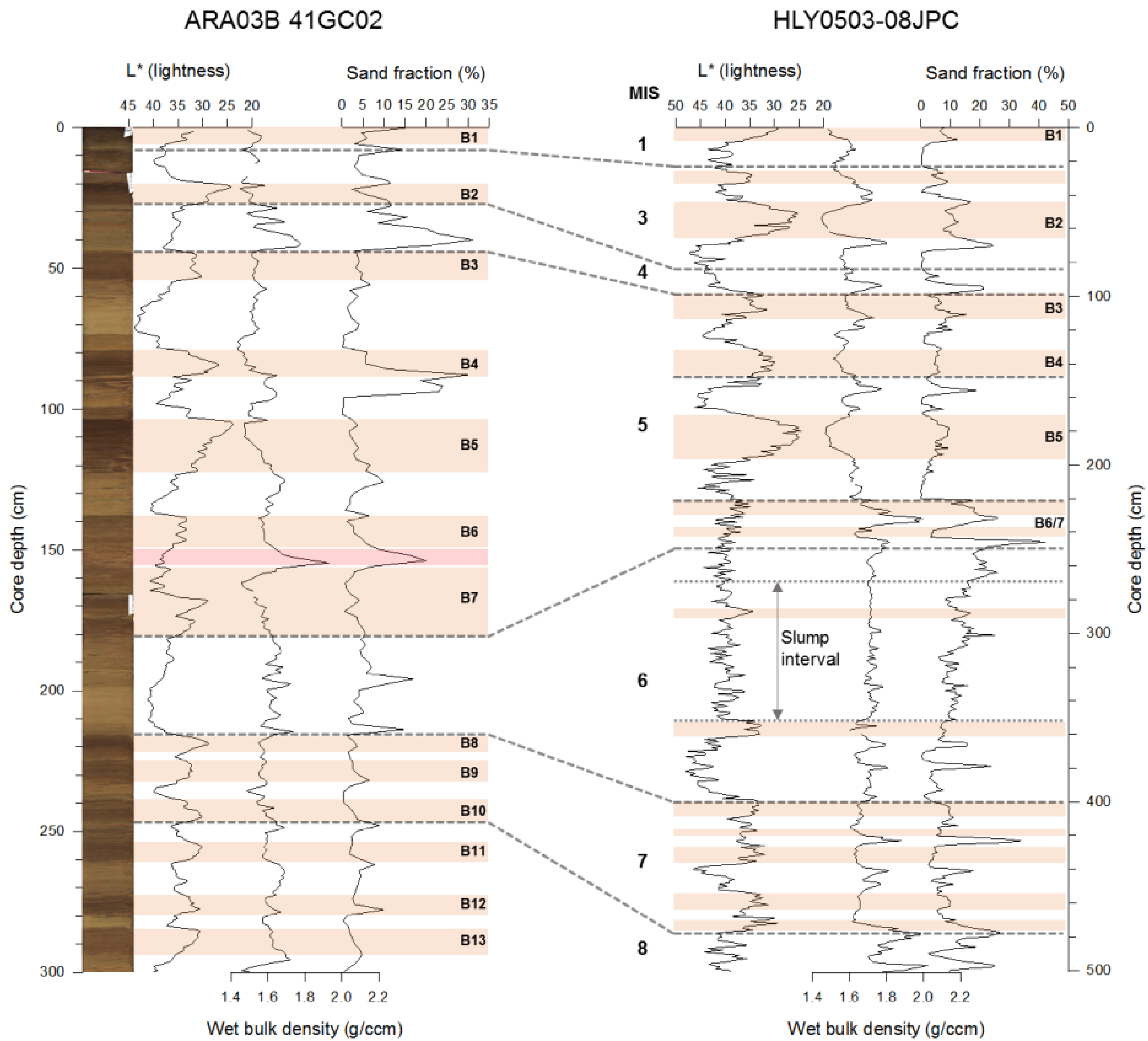
ARA03B 41GC02
HLY0503-08JPC
L* (lightness)
Sand fraction (%)
MIS
Core depth (cm)
Wet bulk density (g/ccm)
B1
B2
B3
B4
B5
B6
B7
B8
B9
B10
B11
B12
B13
B6/7
1
3
4
5
6
7
8
Slump interval

Fig. S1

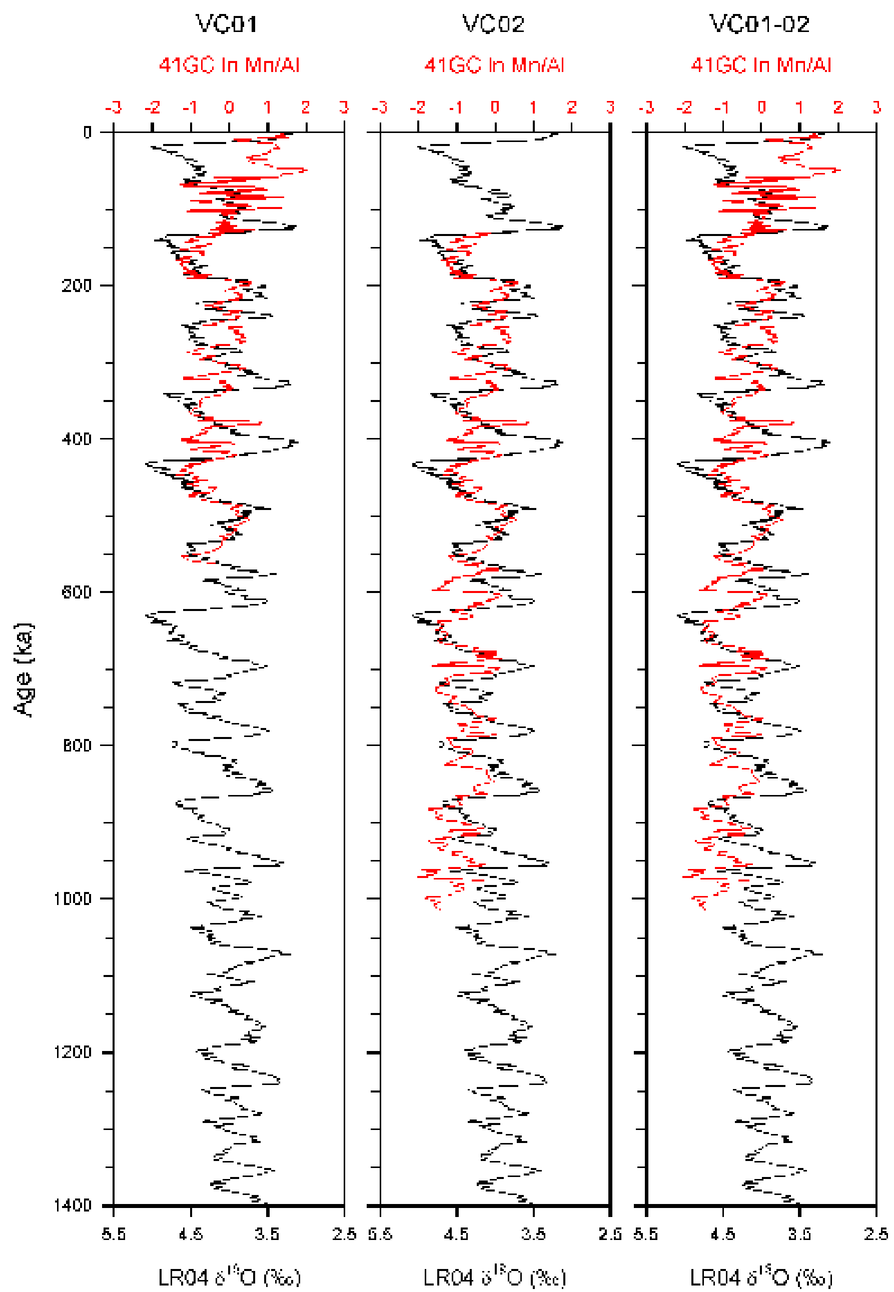

VC01
VC02
VC01-02
41GC ln Mn/Al
-3 -2 -1 0 1 2 3
Age (ka)
0
200
400
600
800
1000
1200
1400
5.5 4.5 3.5 2.5
LR04 δ18O (‰)

Fig. S2

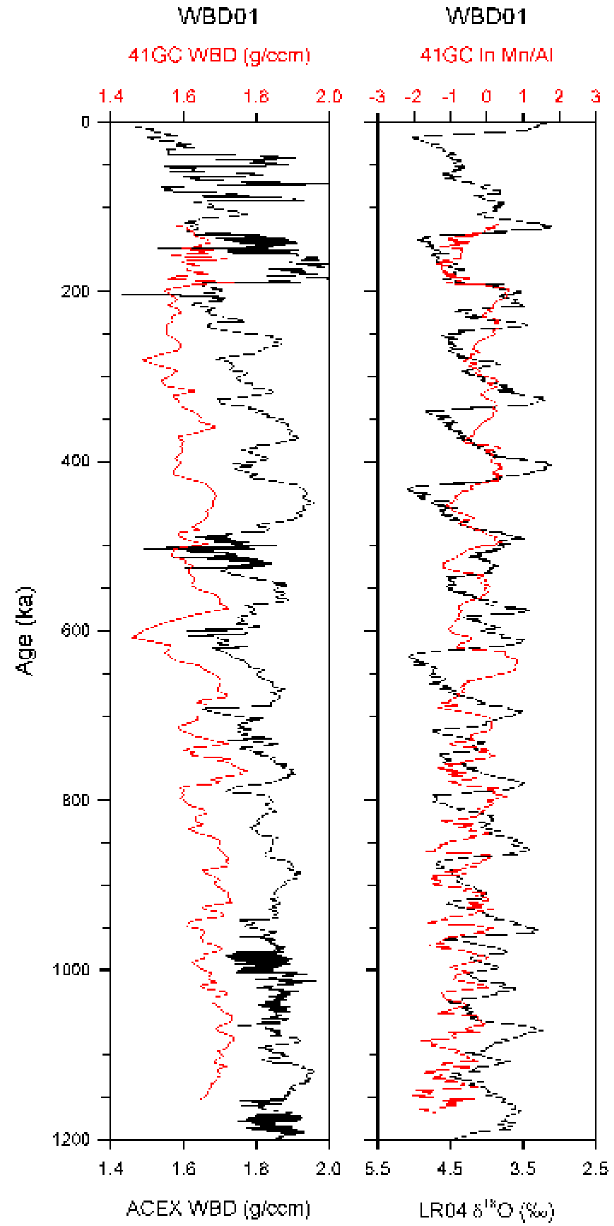
WBD01
41GC WBD (g/ccm)
WBD01
41GC ln Mn/Al
Age (ka)
ACEX WBD (g/ccm)
LR04 δ18O (‰)

Fig. S3

	WBD (g/ccm)	Sand fraction (> 63 µm)	Silt (2–63 µm)	Coarse silt (20–63 µm)	Medium silt (6.3–20 µm)	Fine silt (2–6.3 µm)	Clay (< 2 µm)
WBD	–						
Sand fraction	0.42	–					
Silt	0.71	-0.04	–				
Coarse silt	0.61	0.54	0.32	–			
Medium silt	0.54	-0.01	0.52	0.43	–		
Fine silt	-0.45	-0.48	-0.21	-0.83	-0.25	–	
Clay	-0.58	-0.24	-0.41	-0.66	-0.83	0.28	–

Table S4

MIS boundary	Age (ka)	Core depth (cm)
5/6	130	181
6/7	191	216
7/8	243	246
8/9	300	273
9/10	337	293
10/11	374	301
11/12	424	335
12/13	478	354
13/14	533	363
14/15	563	365
15/16	621	385
16/17	676	392
17/18	712	407
18/19	761	415
19/20	790	419
20/21	814	421
21/22	866	429
22/23	900	438
23/24	917	441
24/25	936	448
25/26	959	451
26/27	970	456
27/28	982	459

Table S5

Table captions

- Table 1. List of AMS ^{14}C dating for ARA03B-41GC02 and 41MUC. No ΔR was applied for calibration using CALIB 7.10.
- Table 2. An overview of the age models based on visual and computational correlations. ln Mn/Al = natural logarithmic Mn/Al ratio, LR04 = LR04 benthic oxygen isotopic stack (Lisiecki and Raymo, 2005).

Figure captions

- Fig. 1. A map showing the study area with the locations of core ARA03B-41GC02 (41GC) and reference cores HLY0503-08JPC (08JPC; Adler et al., 2009), 92/12-1pc (Jakobsson et al., 2000), ACEX (O'Regan et al., 2008), PS72/392-5 (392-5; Stein et al., 2010b), and ARC4-BN05 (BN05; Dong et al., 2017) marked as yellow and green circles, respectively. Glacier limits (white dashed line) during the LGM are modified from Ehlers and Gibbard (2004), Svendsen et al. (2004), and Jakobsson et al. (2013). White arrows correspond to the surface currents of the Arctic Ocean. BG = Beaufort Gyre; TPD = Transpolar Drift; CB = Chukchi Borderland; MR = Mendeleev Ridge; AR = Alpha Ridge; LR = Lomonosov Ridge; GR = Gakkel Ridge.
- Fig. 2. Profiles of color reflectance (L* and a*), XRF-elemental ratio (Mn/Al and Ca/Al), physical properties (magnetic susceptibility (MS) and wet bulk density (WBD)), and sand fraction (>63 μm %) with the core surface image of core ARA03B-41GC02. Brown layers are indicated as B1 to B31 with brown shades. Pinkish shading indicates pink-white (PW) layer.
- Fig. 3. Visual correlation between cores ARA03B-41GC02 and ARC4-BN05 (Dong et al., 2017) mainly based on the presence of brown layers and lithological features including color reflectance (L*), sand fraction, and PW layer.
- Fig. 4. Visual correlation between core ARA03B-41GC02 and LR04 applied beyond the MIS 5/6 boundary. Brown shades indicate brown layers (left panel) and interglacial periods (right panel).
- Fig. 5. Plots of computational correlations between ln Mn/Al of the core ARA03B-41GC02 and LR04.
- Fig. 6. Age-depth plots of visual correlations (VC01-VC02) and computational correlations (MA01-MA05) for core ARA03B-41GC02.
- Fig. 7. Plots of Ca/Al ratios of core ARA03B-41GC02 using age models MA01-05. Blue shades indicate glacial periods.

Supplementary information

- Fig. S1. Visual correlation between cores ARA03B-41GC02 and HLY0503-08JPC (Adler et al., 2009) based on lithological features including color reflectance (L*), WBD, and sand fraction.
- Fig. S2. Plots of ln Mn/Al of core ARA03B-41GC02 versus LR04 based on the age models derived from the visual correlations (VC01, VC02, and the combination of VC01 and VC02, i.e., VC01-02).
- Fig. S3. Computational correlation (WBD01) based on WBD data of core 41GC with those of ACEX (O'Regan et al., 2008) and a plot of ln Mn/Al of core ARA03B-41GC02 versus LR04 based on age model WBD01. Please note that the WBD01 match started from a core depth of ~160 cm corresponding to MIS 5.5 and not from the top of the core.
- Table S4. Correlation coefficients (spearman's r^2) among normalized WBD and grain size parameters. Please note that the sand fraction is weight percent for the bulk weight while the other grain size parameters for the mud fraction are volume percent.
- Table S5. Age-depth tie points at the Marine Isotope Stage (MIS) boundary for ARA03B-41GC derived from VC02 (Figs. 4 and 6).